Computational study of the geometrical influence of grain topography on short crack propagation in AA7XXX series alloys

Materialia

Computational study of the geometrical influence of grain topography on crack propagation in AA7XXX series alloys

--Manuscript Draft--

Manuscript Number:	MTLA-D-23-00208R1
Article Type:	Full Length Article
Keywords:	Fracture Mechanics; Crystal Plasticity Modelling; Spectral Method; Aluminium; Environmentally Assisted Cracking
Corresponding Author:	Cameron James Grant UNITED KINGDOM
First Author:	Cameron James Grant
Order of Authors:	Cameron James Grant
	Y. Aboura
	T. L. Burnett
	P.B. Prangnell
	P. Shanthraj
Abstract:	Intergranular Environmentally-Assisted Cracking (EAC) has recently been reported to be an issue of concern in new-generation 7000 series aluminium alloys, such as AA7085, when exposed to humid air. The cracking process occurs in a highly brittle manner almost exclusively along grain boundaries (GB's) and has been attributed to hydrogen embrittlement, probably by GB decohesion within the stress field at the crack tip. Currently, how the highly heterogeneous grain structures found in these partially recrystallized materials impact the growth behaviour is poorly understood. In particular, there is expected to be a high sensitivity to the grain structure in the transition from initiation to sustained propagation, where the local mechanical driving force is very sensitive to the crack path. Representative Volume Elements, RVE's, with synthetic grain structures have been generated from real microstructure and texture data, so that the effects of important grain structure variables can be explored in crystal-plasticity simulations, to understand the extent to which typical grain-structural features affect the driving force for crack growth. Specifically, by considering the effect of different uncrystallised grain aspect ratios and embedding recrystallised grains in the model, the strain energy release rate has been calculated as a function of crack path. This has revealed large reductions and fluctuations in the driving force for cracks in relation to the local grain structure encountered by the crack tip, which have been estimated by the model.
Suggested Reviewers:	
Opposed Reviewers:	
Response to Reviewers:	We would like to thank the reviewers for their responses, as their feedback was very positive and constructive. We have addressed each of the comments made by the reviewers, and our responses can be found in the resubmitted .pdf file. Reviewer #1's comments largely pertained to small mistakes and formatting issues, whilst Reviewer #2 was primarily seeking further clarification on the volume element sizes, and why precipitate modelling was not included. All the further information and additional figures that Reviewer #2 asked for has been added to the supplementary information document, and their concerns regarding the lack of precipitate modelling have been addressed and clarified.

Cover Letter

Depart of Materials
The University of Manchester
Oxford Street
Manchester M13 9PL

+44(0)161 306 9300
www.manchester.ac.uk

11 May 2023

Ref: Resubmission to Materialia
Ref. No.: MTLA-D-23-00208

Dear Professor Baptiste Gault,

Thank you for providing us an opportunity to revise the paper that we recently submitted for consideration for publication in *Materialia,* entitled; Computational study of the geometrical influence of grain topography on short crack propagation in AA7XXX series alloys'.

We would like to thank the reviewers for their responses, as their feedback was very positive and constructive. We have addressed each of the comments made by the reviewers, and our responses can be found in the attached .pdf document. Reviewer #1's comments largely pertained to small mistakes and formatting issues, whilst Reviewer #2 was primarily seeking further clarification on the volume element sizes, and why precipitate modelling was not included. All the further information and additional figures that Reviewer #2 asked for has been added to the supplementary information document, and their concerns regarding the lack of precipitate modelling have been addressed and clarified.

We would also like to thank you personally for taking the time to read this document, it is greatly appreciated. We look forward to receiving your decision in the near future.

Yours sincerely,

Cameron Grant

Computational study of the geometrical influence of grain topography on short crack propagation in AA7XXX series alloys

C. Grant[a], Y. Aboura[a], T. L. Burnett[a], P.B. Prangnell[a], P. Shanthraj[a]

[a] Department of Materials, The University of Manchester, M13 9PL, UK

Intergranular Environmentally-Assisted Cracking (EAC) has recently been reported to be an issue of concern in new-generation 7000 series aluminium alloys, such as AA7085, when exposed to humid air. The cracking process occurs in a highly brittle manner almost exclusively along grain boundaries (GB's) and has been attributed to hydrogen embrittlement, probably by GB decohesion within the stress field at the crack tip. Currently, how the highly heterogeneous grain structures found in these partially recrystallized materials impact the growth behaviour of microstructurally short cracks is poorly understood. In particular, there is expected to be a high sensitivity to the grain structure in the transition from initiation to sustained propagation, where the local mechanical driving force is very sensitive to the crack path. Volume Elements, VE's, with synthetic grain structures have been generated from real microstructure and texture data, so that the effects of important grain structure variables can be explored in crystal-plasticity simulations, to understand the extent to which typical grain-structural features affect the driving force for short-crack growth. Specifically, by considering the effect of different uncrystallised grain aspect ratios and embedding recrystallised grains in the model, the strain energy release rate has been calculated as a function of crack path. This has revealed large reductions and fluctuations in the driving force for short cracks in relation to the local grain structure encountered by the crack tip, which have been estimated by the model.

Key words: Fracture Mechanics, Crystal Plasticity Modelling, Spectral Method, Aluminium, Environmentally Assisted Cracking

1. Introduction

A new generation of higher zinc level 7000 series Al-Zn-Mg alloys were developed in the 1990's to fulfil aircraft manufacturing requirements, regarding the high-speed machining of larger-integral components [1-3]. The goal of the development of these alloys was to maintain, or increase, the high strength level displayed by more established materials, like AA7050-T7651, and improve their toughness and fatigue crack growth behaviour in thicker-section products, while retaining their good environmental performance [4-6]. This development work led to a range of new alloys being registered by different suppliers such as 7085, 7449, and 7037 [7]. Although this new generation of alloys was designed to surpass standard aviation-industry stress corrosion cracking (SCC) and exfoliation acceptance tests [8], in 2018 the European Aviation Safety Agency (EASA) [9] issued a bulletin reporting that they can be prone to environmentally assisted cracking (EAC) in humid air. Their poor EAC resistance in humid air has since been confirmed in several publications [10], and the cracking process in these alloys has been shown to occur in a highly brittle manner almost exclusively along grain boundaries (GBs). This has been attributed to hydrogen embrittlement, probably by GB decohesion within the stress field at the crack tip [11].

A more complete understanding is thus required of the complex relationships between EAC performance, composition, and microstructure in these important materials [12-17]. Of particular significance is the local chemistry and microstructure of the grain boundaries (GBs) [18], but it has been increasingly recognised that the grain structure, which controls the inter-granular (IG) crack path, is a major factor in determining the crack-growth behaviour [19]. In addition, it is particularly important to improve our understanding of the role of grain structure on the short crack-growth behaviour during the transition from initiation to sustainable cracking, as this is currently largely lacking in the scientific literature. For example, microstructurally short cracks will have a higher sensitivity to local variations in the grain structure and may arrest if deflected at a grain boundary juncture by switching to an inclined grain boundary plane, as this can significantly reduce the tensile opening force, or if they are held back by non-propagating ligaments [20]. In addition, AA7000 series alloy thick-plate products are produced by hot rolling with a relative low reduction ratio (50-75%) and are thermomechanically processed under conditions designed to minimise recrystallization during the subsequent high temperature solution heat treatment step,

required by their precipitation hardening treatment [21]. As finished products, they therefore generally contain a heterogeneous partially recrystallized grain structure consisting of approximately 10-20% irregular recrystallized grains, along with an uncrystallised matrix of coarse-fibrous grains elongated in the rolling plane [39].

A primary goal of this paper is thus to address an important aspect of this complex problem, by providing more insight into how the crack path can impact the early-stage mechanical driving force for microstructurally short EAC cracks in materials with such heterogeneous grain structures. Although, topographic modelling of long stress corrosion cracks has shown that the effective average stress intensity (K_1) at the crack tip can be reduced by as much as 50%, by deviation of the crack path from an ideal plane [22], current knowledge surrounding short crack growth is limited to fatigue cracking, which is generally not intergranular. Research regarding short fatigue crack-growth behaviour in aluminium alloys acknowledges that when microstructural effects are accounted for their rates are subject to considerable scatter [23], but provides little quantification of the source of this scatter, in relation to the microstructure descriptive parameters. Jones et al. [24-25] have also drawn attention to the inappropriate use of K_{Max} values when modelling crack growth rates, since calculations of K_1 generally rely on simple geometrical models of the crack shape, which are not appropriate for quantifying the crack driving forces of microstructurally short cracks.

A particularly clear illustration of the extent to which a material's microstructure and the test geometry can influence the magnitude of crack driving forces has been provided by Euesden et al. [26]. It is notable that in their data large through-thickness cracks growing with a decreasing driving force in double cantilever DCB tests stopped at a threshold $K_{1,EAC}$ far higher than that below which short naturally-initiated cracks grew from polished surfaces in 4 point bend (4PB) tests, when modelled with simple linear-elastic calculations based on an idealised crack geometry. In addition, the short crack data revealed a large scatter in growth velocity, which reduced notably when the crack length became significantly larger than the material's grain size.

Alongside experimental short crack initiation studies, fracture mechanical approaches to short cracks and the simulation of short crack behaviour is an active research topic [27]. For example, Lubich et al. [28] have conducted finite-element (FE) analyses of crack-tip opening displacements for microstructurally short cracks, and discovered that the calculated values were significantly influenced by the local grain structure and the presence of softer oriented grains. Wilson et al. [29] have also employed crystal plasticity simulations with the eX-tended finite-element method (XFEM), to investigate grain boundary interactions for microstructurally short cracks, where dislocation stored energy values were used to quantify the driving forces through a simple bicrystal microstructure.

More recently, crystal plasticity spectral element modelling using synthetic microstructures has become an important tool for simulating the fracture behaviour of metal alloys [30], and has the benefit over traditional linear-elastic fracture mechanics in that it can allow the effects of microstructure heterogeneity to be systematically explored, by reconstructing the grain structure of real materials using volume elements (VE's). DREAM.3D has been used extensively throughout the scientific literature to construct synthetic microstructures for use in crystal plasticity simulations [31]. De Francisco et al. used DREAM.3D to produce cylindrical synthetic microstructures in a cohesive zone finite element model, with the goal of mimicking the HEAC behaviour during crack initiation and microstructurally short cracking of AA7449-T7651 in moist air [32]. Diehl et al. have also used DREAM.3D to produce synthetic cold-rolled microstructures for an Fe–23Mn–1.5Al–0.3C twinning-induced plasticity steel, which were used in combination with the DAMASK spectral solver to investigate the mechanical responses of different microstructures [33].

While microstructure-based crystal plasticity simulations can provide valuable insight into the nature of short crack growth and propagation, previous studies on the crack driving forces for short cracks are largely qualitative and performed on greatly simplified microstructures that are non-representative of real materials [23]. There are also few quantitative studies available which systematically consider the effect of variation of important features, such as grain morphology and heterogeneity and their implications for the crack driving forces for microstructurally short cracks. Hence, this paper aims to provide more insight into how statistically different grain structures, replicated from real materials, can impact crack driving forces in the practically important context of improving our understanding of the EAC behaviour of high strength 7000 series aluminium alloys, which have particularly heterogeneous partially recrystallised grain structures. This was achieved by creating synthetic grain structures

using measured grain and texture data from real materials and then systematically varying the grain morphology, as well as embedding 'recrystallised' grains into the models. Crystal plasticity simulations were then used to explore the effects that grain morphology had on the strain energy release rate for different inter-granular fracture paths.

2. Computational Methods

Crystal plasticity modelling continues to gain considerable momentum in the scientific community, at least in part thanks to the development of the Düsseldorf Advanced Material Simulation Kit (DAMASK), a multi-physics software tool for conducting advanced microstructure–property simulations. The capabilities of DAMASK are described in the software overview paper [34], together with numerous usage examples. The following crystal plasticity model was first developed by Hutchinson [35], before being extended by Kalidindi [36].

2.1 DAMASK Phenomenological Crystal Plasticity Model

Consider a given mathematical domain of interest $\mathcal{B}_0 \in \mathbb{R}^3$, with boundary $\partial\mathcal{B}_0$. The deformation resulting from an applied loading, defined by a field $\boldsymbol{\chi}(\mathbf{x})$: $\mathbf{x} \in \mathcal{B}_0 \rightarrow \mathbf{y} \in \mathcal{B}$ maps points x in the reference configuration to points y in the deformed configuration $\mathcal{B}$. The total deformation gradient, given by $\mathbf{F} = \partial\boldsymbol{\chi}/\,\partial\mathbf{x}$, is multiplicatively decomposed into elastic and plastic components as $\mathbf{F} = \mathbf{F}_e\mathbf{F}_p$. An anisotropic stiffness tensor, $\mathbb{C}$, relates the elastic deformation gradient, $\mathbf{F}_e$ to the second Piola-Kirchhoff stress tensor, $\mathbf{S} = \mathbb{C}\left(\mathbf{F}_e^T\mathbf{F}_e - \mathbf{I}\right)/2$. The plastic velocity gradient, $\mathbf{L}_p = \dot{\mathbf{F}}_p\mathbf{F}_p^{-1}$, is then driven by $\mathbf{S}$, by virtue of the chosen crystal plasticity model.

Since the plasticity of crystalline metals occur on specific slip systems, dependant on their lattice structure, this gives the following definition for the plastic velocity gradient, L_p:

$$\mathbf{L}_p = \dot{\mathbf{F}}_p\mathbf{F}_p^{-1} = \sum_{\alpha} \dot{\gamma}^{\alpha}\, \mathbf{s}^{\alpha} \otimes \mathbf{n}^{\alpha}$$

The plastic velocity gradient, L_p, can then be calculated by summing over the individual shear contributions, $\dot{\gamma}^{\alpha}$, on those slip systems, α. Where s^{α} and n^{α} are unit vectors along the slip direction and slip plane normal, respectively. The plasticity constitutive equations are as follows:

$$\dot{\gamma}^{\alpha} = \dot{\gamma}^{0} \left|\frac{\tau^{\alpha}}{g^{\alpha}}\right|^{n} sgn(\tau^{\alpha})$$

Where the slip resistances present on each slip system, g^{α}, evolve asymptotically towards g^{∞} with shear γ^{β} in accordance with the following relationship:

$$\dot{g}^{\alpha} = \dot{\gamma}^{\alpha} h_0 \left|1 - \frac{g^{\beta}}{g_{\infty}}\right|^{\alpha} sgn\left(1 - \frac{g^{\beta}}{g_{\infty}}\right) h_{\alpha\beta}$$

$\{\beta \in \mathbb{Z}: 1 \leq \beta \leq 12\}$, h_0 and a are specified parameters, and the interactions of different slip systems are captured by the hardening matrix $h_{\alpha\beta}$.

The elastic constants for aluminium are well known and were taken directly from the literature [37], which alongside the other material CRSS and hardening parameters (n, g_0, g_∞, h_0, a, $\dot{\varepsilon}_0$) used are provided in Table 1. A soft dilatational 'buffer' material was added to break up the DAMASK grid solver's periodic boundary conditions, which results in almost zero stress conditions where required [38].

Table 1: Material parameters; elastic constants C_{ij}, reference strain rate $\dot{\varepsilon}_0$, stress exponent n, initial and saturation flowstress g_0 and g_∞, and hardening parameters h_0 and a.

DAMASK - AA7085 Refined Material Parameters

Parameter	Aluminium	Dilatational (Air)	Units
C_{11}	106.75	10	GPa
C_{12}	604.1	0	GPa
C_{44}	283.4	5	GPa
N	20	20	
g_0	155	0.3	MPa
g_∞	160	0.6	MPa
a	2	2	
h_0	200	1	MPa
$\dot{\varepsilon}_0$	10^{-3}	10^{-3}	s^{-1}

2.2 Volume Element (VE) Creation

Each Volume Element (VE) used in this study was constructed to be statistically representative of a typical AA7085-T7651 thick-plate product's grain structure. The models were designed to represent the early stages of a propagating inter-granular EAC crack after its initiation. However, they could equally be thought of as representing a small increment of the crack front of a larger crack during EAC or SCC.

To include representative grain structures in the model, DREAM.3D [31] was employed to generate a range of 3D synthetic microstructures, using statistical grain and texture information measured from a 140 mm thick AA7085 alloy commercial aerospace plate by electron back-scatter diffraction (EBSD). This was obtained by performing EBSD characterization on the L-ST (plate rolling and normal directions; RD-ND) and LT-ST (plate normal and transverse directions; ND-TD) planes of the rolled plate at the T/4 position, with large map areas, to collect statistically valid data from over 1500 grains. The average grain size area was 5000 μm^2, giving an equivalent circular diameter of 40 μm, and most of the plate contained fibrous grains elongated in the rolling direction with an L/ST grain aspect ratio of 4.5. The heat-treated plate also contained a low volume fraction of ~16% of irregular shaped recrystallised grains [39]. However, these were not included in the 'standard' VE which was designed to replicate the average fibrous grain size and shape statistics. The size of the VE's was restricted by the available computational resources, but each volume element was made as large as practically possible and contained approximately 100 grains [69]. The texture of thick rolled 7085 plates consist of weak rolling and cube recrystallization components with a maximum intensity of < 3 MRD and was therefore not varied in this study.

The parameters used to generate the standard model with an equivalent grain spherical diameter (ESD) probability distribution in DREAM.3D, which reproduced the AA7085 grain structure in the experimental EBSD data, are provided in Table 2. These parameters are used to generate a probability density function, from which the user can generate the necessary statistics that describe the wanted microstructure. Additional figures detailing the convergence of the synthetic microstructural statistics with the experimental EBSD statistics can be found in the supplementary information. Each VE had dimensions of 448 x 144 x 96 voxels, which for cubic voxels of width 3.1 μm resulted in a volume element with dimensions of 1400x450x300 μm^3, (L x LT x ST). The crystallographic texture of the hot rolled material contained mainly weak rolling components, but was also imported into DREAM.3D, using the orientation distribution function (ODF) calculated from the experimental EBSD data performed by AZtecCrystal [40]. The equivalent mean size diameter (ESD) that governs the size of the grains contained within the VE, and the parameter values specifying the ESD probability distribution that have been used throughout, are defined in Table 2. The simulated VE's were loaded in the ST direction at a constant strain rate of

$\dot{\varepsilon}_0 = 1\text{x}10^{-3}\ s^{-1}$, and had periodic boundary conditions in the L and the ST directions. A dilatational buffer region, with the material properties of air, was used to break up the periodic boundary conditions in the LT direction and to represent a cracked GB.

Table 2: The parameters used for the synthetic microstructure generation by DREAM.3D. The average value of the lognormal grain size distribution, μ, is the average value of log(ESD). The standard deviation of the lognormal grain size distribution, σ, is not the standard deviation of the actual feature size distribution, but of the log(ESD) values. The parameters μ, min and max cut off, are given for an equivalent sphere diameter in μm.

DREAM.3D: Probability Density Function Values

Parameter	Value
Mean Equivalent Sphere Diameter (ESD)	41.68
μ	2.75
σ	1.4
Bin Step Size	2
Min/Max Cut Off	3/1.75
Bin Step Size	2

Although each VE was constructed to be statistically representative of a typical thick plate AA7085-T7651 alloy's grain structure, it should be recognised that although multiple instantiations will produce very similar microstructural features and characteristics, no two VE's created will be identical.

This standard model was subsequently systematically altered to perform three different case studies that varied:

i. The grain aspect ratio in LT-ST, to explore the average effect on the strain energy release rate of changing the crack surface corrugation.
ii. The effect of a plane strain rolling reduction in the range (i.e. 50-75% [41]) of thick aerospace plates, mimicked by changing the grain aspect ratio in the L-ST plane, while keeping the grain width in the LT direction constant.
iii. The size of an equiaxed 'recrystallised grain' inserted in the centre of the standard unrecrystallised VE model

In addition to this, a 'bicrystal' model was created containing a single planar grain boundary, lying normal to the loading direction along its centre line, to provide a baseline-planar crack that was unaffected by grain boundary topography. Case i. was performed with a more computationally efficient large crack advance increment of 156 μm, to estimate the average effect on the strain energy release rate, G, whereas ii. and iii. were performed with a small crack advance increment of only 31 μm to explore both the average and local effects of grain structure interactions during crack growth.

2.3 Model Setup

The modelling set-up, employed to quantify the effect of grain structure on the crack driving forces, consisted of a series of static crack simulations with an incrementally increased crack length. A similar incremental approach has been adopted by other authors [42], and has the advantage that it can emulate crack propagation without the complication of performing dynamical fracture modelling, which in the EAC case is problematic because the physics of the crack propagation mechanism and the controlling parameters are currently poorly understood [43]. Information regarding the crack driving forces was then obtained by considering the difference in total strain energy and crack surface area for a given VE, from one simulation to the next.

To replicate the inter-granular hydrogen embrittlement EAC process observed in experiments, once a VE had been generated, the crack was created by changing the GB properties in the VE at the desired location to values associated with air. The cracks were artificially propagated along the grain boundaries closest to the rolling direction (in the L-LT plane), which is the most susceptible orientation in aluminium plates [44], with a straight

crack front. In reality, EAC cracks will 'feel' their way through a material by advancing more quickly, or slowly, locally depending on the local driving forces and GB resistance, leading to an irregular crack front [45]. However, on the scale of a small VE, this simplification is a reasonable assumption. The fracture propagation path was predefined and selected based on the path of least microstructural resistance that minimised grain boundary deflections. From comparison to experimental data this gave very realistic crack paths, which closely replicated those of a real material (Figure 1). Two resolutions of crack increment were used – one coarse (156 μm) to obtain the average response of the VE, which required at least 8 incremental static crack simulations per VE, and one much finer with only a 31 μm advance, to study the local effect of grain topography. This higher resolution incremental crack advance required considerably more computational effort, as it necessitated 36 static crack simulations per VE. The cracks were not propagated through the entire length of the VE in the L direction, they instead stopped approximately 350 μm before the end of the VE. This was done in an attempt to minimise any interaction the crack might have with itself, via the periodic boundary conditions present in the L direction. The minimum simulated crack length was chosen to be 200 μm, as the crack length is similar to the size of the microstructural features that we're investigating. To investigate crack sizes smaller than this, the cracks would be too heavily influenced by other microstructural features that are not included in the model, such as regions of high dislocation density, precipitates, or pores. Regarding the maximum length, experimental evidence suggests that short cracks begin to transition to long cracks at about the 1mm mark, as shown by Euesden et al [26]. In addition to this, the overall size of the VE's impacts computational performance, placing a further upper limit on the crack lengths.

The Strain Energy Release Rate, G, was the preferred fracture mechanics parameter used to quantify the crack driving force. This is because when calculating Stress Intensity Factors (SIF's), the dependency on the geometry of the body, the size, shape, and position of the crack, as well as the loading conditions must be considered. The strain energy release rate does not share such complex dependencies and is therefore more suitable to fracture mechanics problems where the crack geometry is non-trivial. The energy release rate, G, is defined as the energy dissipated during fracture per unit of newly created fracture surface area, s. The total potential energy, Π, can be written in terms of the total strain energy Ω, surface traction **t**, displacement **u** and body force **b**, by [46]:

$$\Pi = \Omega - \left\{ \int_S \mathbf{t} \cdot \mathbf{u} dS + \int_V \mathbf{b} \cdot \mathbf{u} dV \right\}$$

This leads to the following definition for the strain energy release rate, G, in the absence of body forces or surface tractions:

$$\mathrm{G} = -\frac{\partial \Omega}{\partial s}$$

To obtain the strain energy release rate, the strain energy density, ω , must first be defined, which is given by the following tensor contraction [47]:

$$\omega = \frac{1}{2} \mathbf{S} : \boldsymbol{\gamma}_e$$

Where **S** is the second Piola-Kirchhoff stress tensor, and $\boldsymbol{\gamma}_e$ is the elastic component of the Green-Lagrange strain tensor. The total strain energy, Ω, can then be obtained by integrating the strain energy density over the volume:

$$\Omega = \int \omega dV = \frac{1}{2} \int \mathbf{S} : \boldsymbol{\gamma}_e dV$$

The difference in strain energy can then be calculated between two adjacent static crack simulations, and divided by the change in crack surface area to provide the desired strain energy release rate. The crack surface area values were obtained in Paraview, by using the `extract surface', `cell size', and `integrate variables' filters on the fracture surface material ID.

Normalised values of G are provided below, scaled relative to the maximum value of strain energy release rate obtained for a crack propagating in the planar boundary bicrystal model. This is because without a dynamic cracking model, based on accurate physics, absolute values of G are arbitrarily dependent on the load applied to the model. To make the plasticity at the crack tip realistic, the applied load was set to 75% of the materials yield stress, which is typical for EAC static load tests [48]. An additional figure detailing the planar boundary bicrystal model and its boundary conditions has been added to the supplementary information.

2.4 Material Parameter Calibration

Prior to investigating the crack driving forces, the plasticity parameters used in the model for the specific alloy and microstructure of interest were calibrated. 3 standard volume elements were created in accordance with the method outline above, loaded in tension parallel to ST, and their mechanical response compared to measured stress-strain curves from dry air tensile ST tests of the material being simulated. The aluminium plasticity parameters shown in Table 1 were then slightly adjusted until convergence with the experimental stress-strain data was achieved. A comparison of the stress-strain curves measured in the ST, crack opening, direction and the equivalent Crystal Plasticity model prediction after parametric refinement is provided in Figure 1, showing excellent agreement. The optimised material parameters obtained after this calibration process are displayed in Table 1. The material parameters shown in Table 1 for the dilatational air layer were taken from Maiti et al[38].

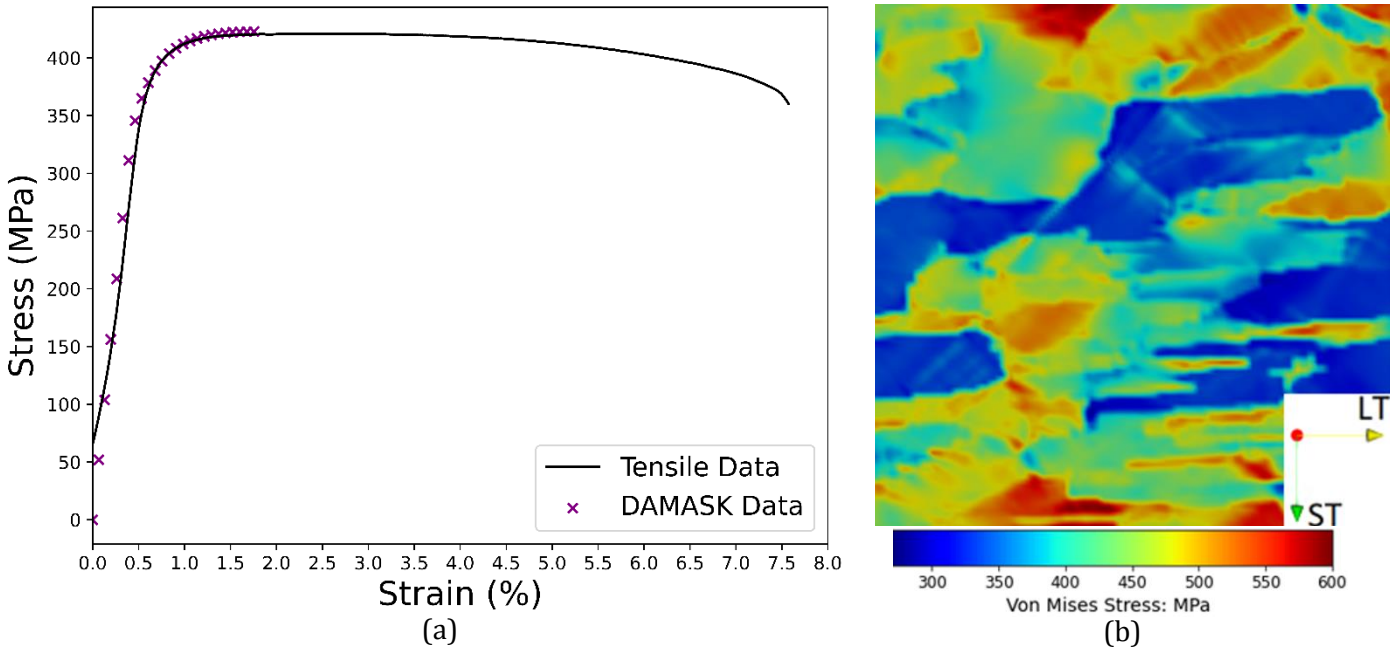

(a) (b)

Figure 1: (a) Measured ST tensile stress-strain curve for AA7085 obtained at a test temperature of 70°C, illustrating the good agreement with the simulated VE after optimisation of the CRSS slip parameters. In (b) an example slice from the VE's central plane can be seen after 2% strain showing the Von Mises stress distribution.

3. Results

3.1 Typical EAC crack in thick plates

The typical brittle inter-granular EAC behaviour observed for the commercial material that we wish to simulate is shown in Figure 2, adapted from [20]. Figure 2 depicts an intergranular crack growing in an AA7085 double cantilever beam DCB sample in a conventional 2D EBSD map. A smaller 3D volume produced by serial sectioning in a laser FIB, in Figure 2(b) highlights the complexity of the crack-path topography, which is caused by the limited (50-70%) rolling reduction used for thick plate products and the heterogeneous partial recrystallization that occurs in the Zr depleted inter-dendritic regions [49]. Key features seen in this example that need to be captured in the model so that their influence on the strain energy release rate can be estimated include; i) the inter-granular

nature of the crack path and its complex topography as it tries to follow the elongated fibrous grain structure in the rolled plate; ii) bifurcation, or crack branching where segments of the crack meet a grain juncture and start to propagate on a different plane, and iii) the greater level of deflection when a crack encounters a recrystallised grain.

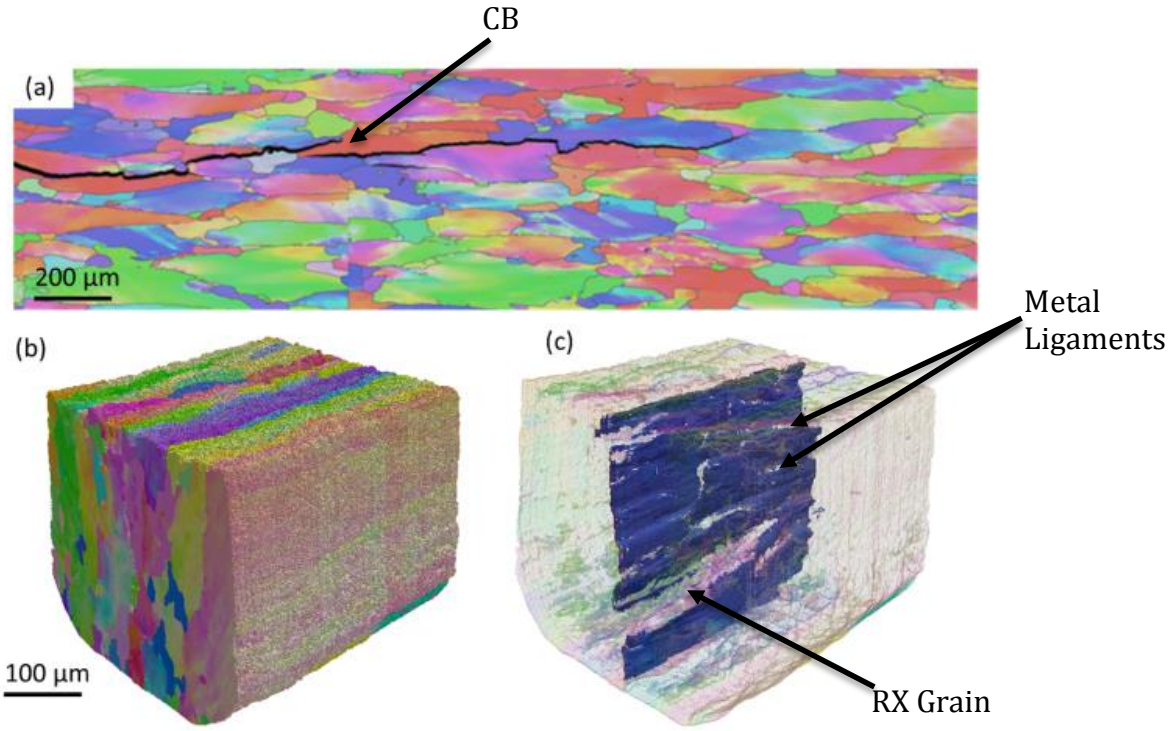

Figure 2: Typical intergranular cracks growing in an AA7085-T7651 DCB sample seen (a) in a conventional 2D EBSD map that provides crystallographic information of the materials grain structure and (b) a smaller 3D volume produced by serial sectioning in a laser-tri-beam Plasma FIB, which highlights the complexity of the crack path topography in a real hot-rolled plate; adapted from the work of Garner et al. [20]. An example of crack branching (CB), where segments of the crack meet a grain juncture and start to propagate on a different plane, has been labelled in (a). The small gaps present in the fracture surface shown in (c) are metal ligaments and have also been labelled, alongside a large gap in the fracture surface, which was caused by a recrystallised grain.

3.2 Effects of the grain structure on the average strain energy release rate

Average effect of grain topography

Before examining local microstructure influences on G, the average strain energy release rates in the VEs were evaluated to understand the overall effect of thick plate grain-structure morphologies on the crack driving forces. The strain energy release rates calculated from VE simulations containing different grain structures, carried out with a relatively coarse-scale 156 µm crack advance increment, are compared in Figure 3 as a function of increasing crack extension. In Figure 3 the values for G have been normalised relative to the maximum experienced by the small starting crack in the bicrystal baseline VE, and a lower relative strain energy released per unit area reflects greater difficulty of crack propagation and a lower mechanical driving force for EAC. A typical example of the sequence of crack extension modelled in a ‘standard’ grain structure VE is also shown in Figure 4, where it can be seen qualitatively that the behaviour of the simulation appears in good agreement with the experimental images shown in Figure 1. In Figure 3 all the results have a slight linear-negative slope because the total strain energy in the VE gradually reduces as the growing crack progressively elastically relaxes the model.

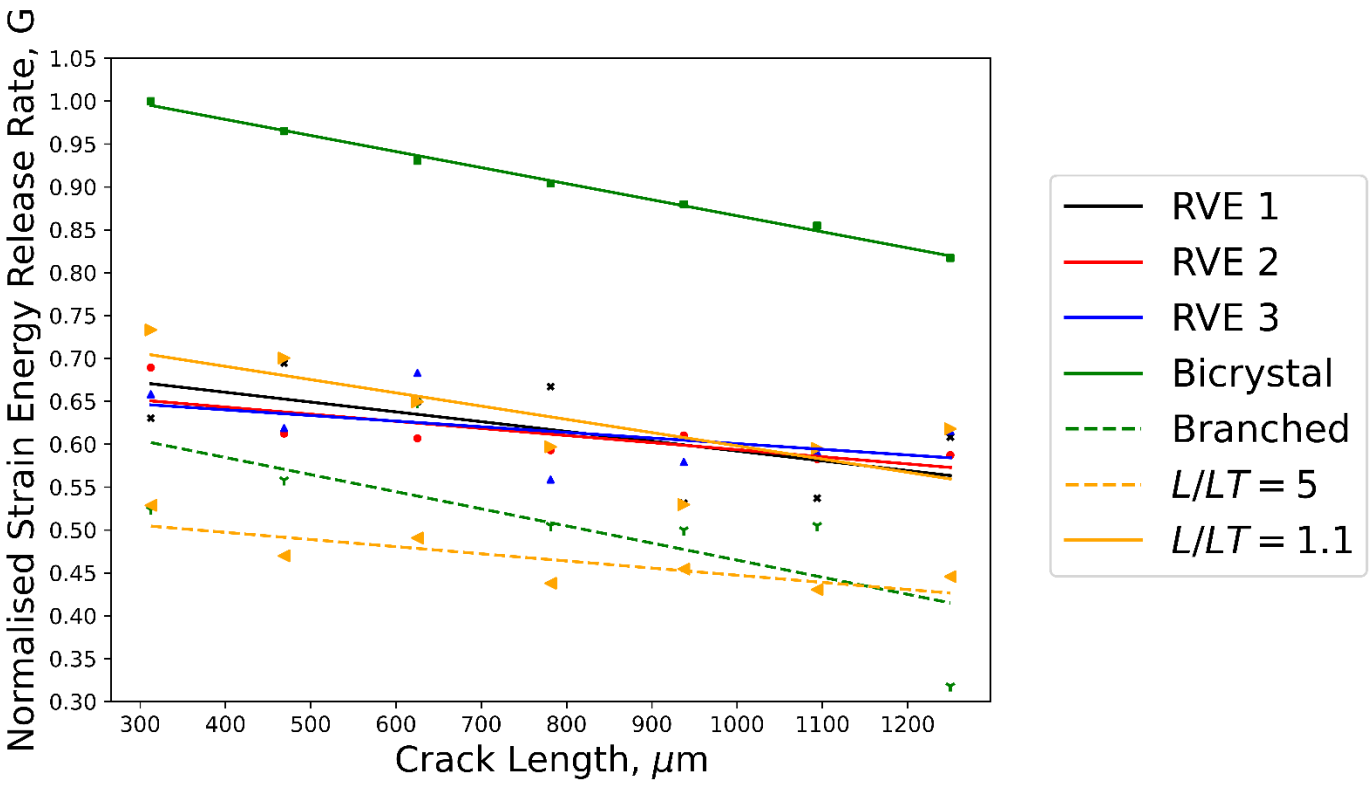

Figure 3: Strain energy release rate, G_n, normalised relative to the planar baseline planar-bicrystal crack, calculated with a coarse crack advance increment in the standard grain structure compared to 3 standard grain structure VEs and VEs with two different levels of fracture surface corrugation and crack branching.

The average strain energy release rates are first compared for cracks grown in three VE's produced with the same standard grain-structure parameters, and VE's 1, 2, and 3 have average G_n values of 0.617, 0.611 and 0.614, respectively. This means that replacing a given VE with another that is individually different, but statistically identical, only produces a minimal <1% change in the calculated average strain energy release rate, suggesting the VE's used are large enough to average out `point-to-point' local effects over the course of the full propagation path, which leads to near-identical average strain energy release rates when the polycrystal grain structures are all statistically equivalent. This low variation gives confidence that the VE volume relative to the grain size employed is sufficient to give repeatable results with different synthetic grain structures.

In terms of the overall effect of grain structure on the driving force for EAC, the primary observation from Figure 3 is that, when averaged over the full VE crack path, there is a large overall difference between the energy released by growing the baseline planar-crack and that of the simulated structures that include grain topography. For example, in the standard simulated polycrystalline microstructures, the driving force to propagate a crack through the VE was on average 30% lower than for the planar bi-crystal case, even when bifurcation is not taken into account. Thus, when GB topography is considered, even though the crack is propagating in the easiest growth direction in the plate (i.e. parallel to the rolling direction), there is still a significant reduction in the average driving force relative to that assumed with a planar crack.

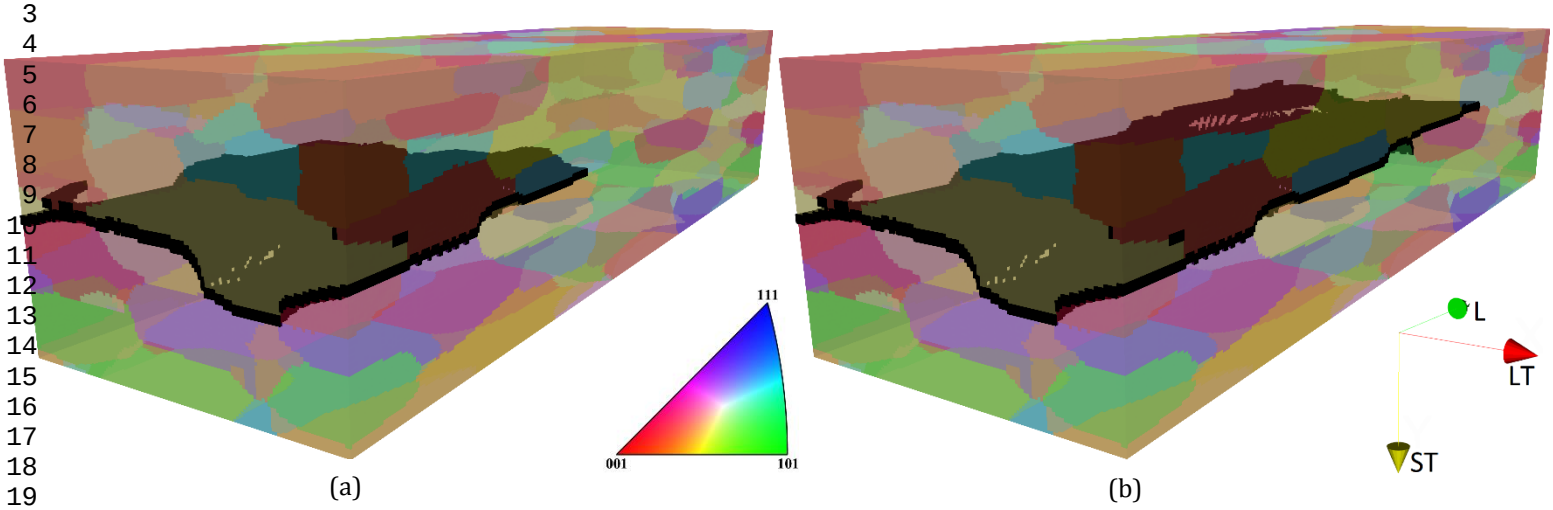

(a) (b)

Figure 4: Example of a simulated crack developing in a typical VE used to represent the 'standard' measured average grain structure of a AA7085 thick plate Alloy. The grains can be seen by their orientation-colour contrast in the Inverse Pole Figure (ND) IPF map. The fracture surface is shown in black. Each VE contained a total of 101 grains, and the crack length shown increases from 468.75 μm in (a), to 937.5 μm in (b).

The effect of changing the fracture surface roughness is also shown in Figure 3, where the corrugation is artificially modified by reducing the grain aspect ratios in the LT-L plane from 5 to 1.1, while the average grain length in the rolling direction (L) was kept constant. Examples of the cracks in the VE's used to produce these datasets are provided in Figure 5, where it can be seen that a higher L/LT ratio gives significantly greater crack topography. These simulations clearly show that the average calculated strain energy release-rates to propagate a crack are lower for the case of a more corrugated fracture surface (L/LT = 5), reflecting a reduced driving force for crack propagation, and are higher with a smoother fracture surface when the grains have a flatter more pancake-like morphology. In addition, the simulations show that, for the case with the highest level of corrugation, the average driving force for crack growth would be expected to be ~ 50% below that for a planar crack, as is assumed in conventional engineering fracture mechanics. This difference is substantial and indicates that the average crack driving forces are much lower in a polycrystal, even when it has a grain structure elongated in the rolling plane, even when bifurcation and ligament formation is not taken into account.

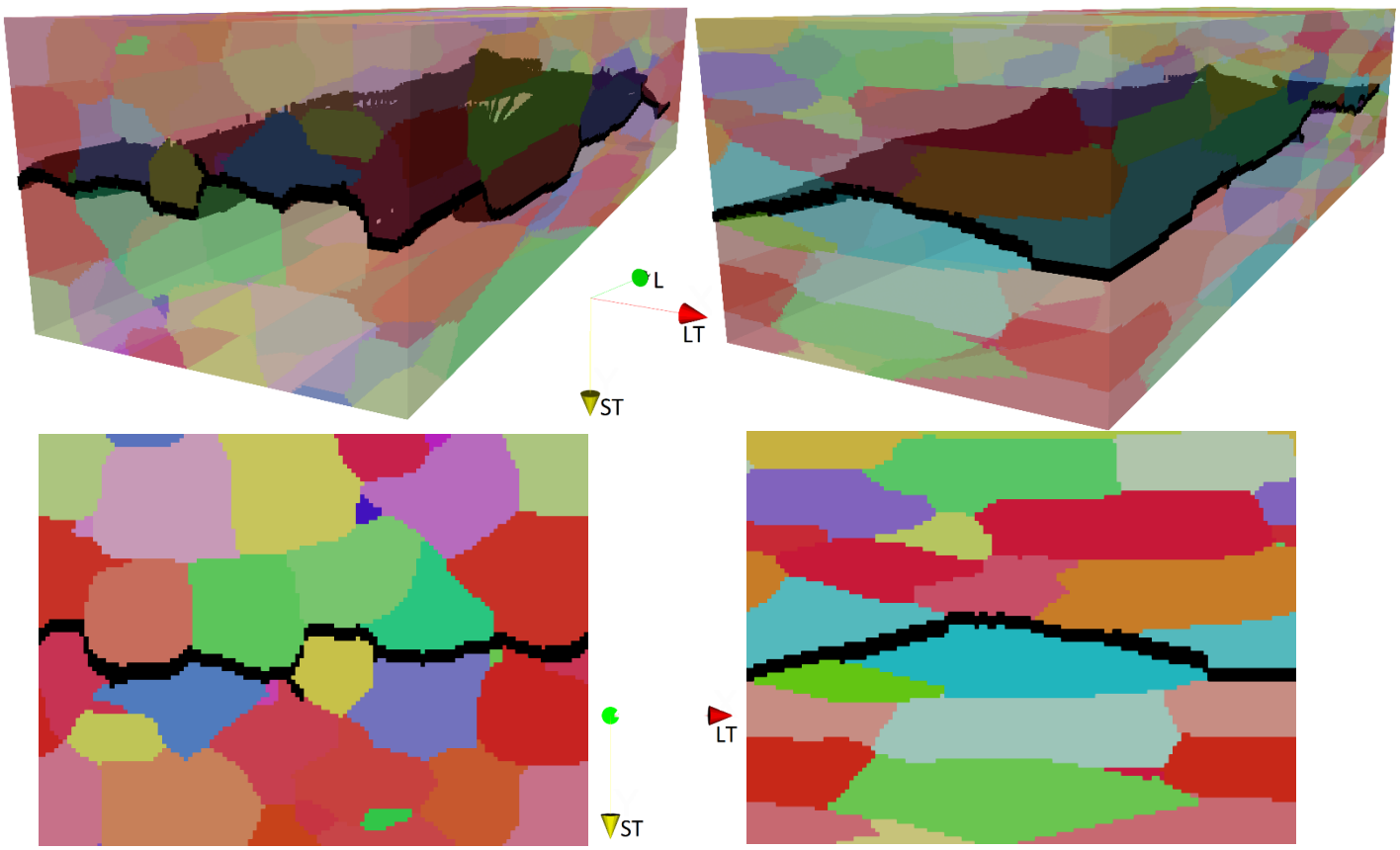

(a) L/LT = 5 (b) L/LT = 1.1

Figure 5: 3D semi-transparent and 2D (LT-ST plane) section views of cracks in VEs with different L/LT grain aspect ratio's of (a) 5 and (b) 1.1, depicting the impact on the overall fracture surface topography.

In addition to the strong effect of GB topography, inter-granular cracks in real materials can frequently bifurcate when they encounter grain boundary junctions (Figure 2). An addtional simulation was therefore performed using the standard grain structure VE where the crack was allowed to split as it encountered every GB juncture when there was ambiguity in the choice of crack path. Each secondary crack branch was then allowed to propagate until it reached the next grain boundary junction it encountered, where it was arrested. The effect of these simplified simulated crack branching events on G_n is illustrated in Figure 3, and the crack path in this VE is shown in Figure 6. In Figure 3, the strain energy release rate for the branched crack can be seen to sit significantly below that of the other non-branching cracks performed in statistically equivalent microstructures. When averaged over the entire volume, the value of G_n for this simulation was calculated to be 17% lower than calculated for identical VE's performed without branching. When combined with the effects of grain topography, this increased the average reduction in energy release rate relative to a planar crack for the standard model by 44%. However, locally, when crack deflection took place the strain energy release-rate was much more strongly affected, as will be explored further below with a higher resolution crack-advance increment.

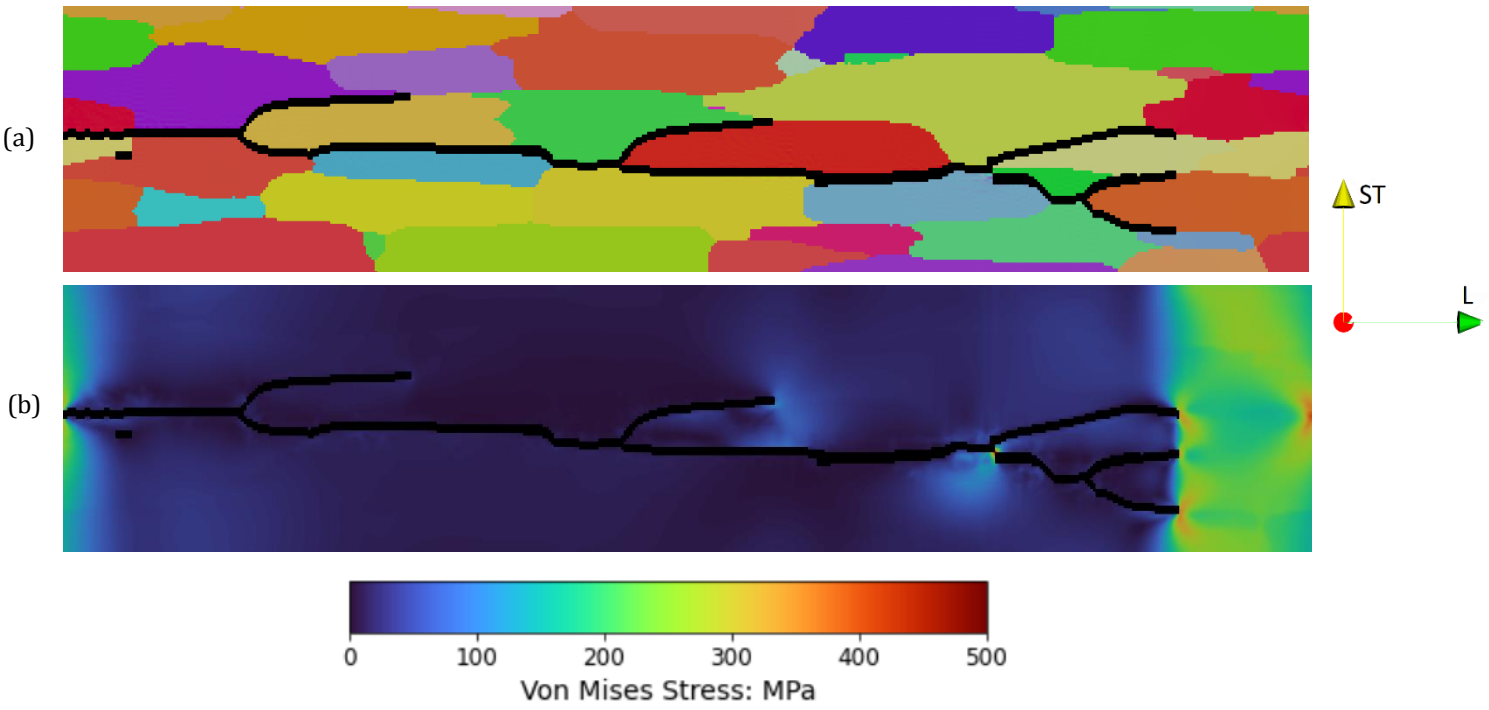

Figure 6: (a) Example of a VE with the standard grain structure in which branching was allowed to take place at every GB juncture where there was ambiguity in the choice of crack path; (a) the synthetic grain structure, as viewed in the L-ST plane and (b) the Von Mises stress distribution. In (b) slight edge effects due to the periodic boundary conditions can be seen.

3.3 Higher resolution simulations of grain interactions

Although this was computationally more expensive, further simulations were performed with a much smaller crack advance increment of 31 μm, which gave several increments per grain. This higher crack extension resolution was used to explore the effect of individual transient microstructure events, such as when the crack encountered a grain juncture. These higher resolution crack advance simulations were applied to the two important case studies introduced above; ii) where the effect of varying the rolling reduction on the grain structure was simulated, and iii) where an equiaxed 'recrystallised' grain was embedded in a fibrous matrix.

Effect of rolling reduction

To ascertain how sensitive the average and local crack driving force was to thick-plate rolled grain geometries, simulations were performed with VE's designed to emulate three different rolling reductions, ranging from a baseline, with zero rolling reduction and equiaxed grains, to 50% and 75% reduction ratios. The 50% and 75% reductions were selected as they are representative of the reduction range applied to 75 – 150 mm thick 7xxx aluminium alloy plates during hot rolling from DC cast billets [50]. This was carried out by changing the grain aspect ratio in the L-ST (RD-ND) plane relative to the measured grain structure data distribution, while keeping the width of the grains in the LT (TD) direction constant, to replicate the effect of equivalent levels of plane strain compression. Illustrations of cracks growing in VE's for these three conditions are shown in Figure 7.

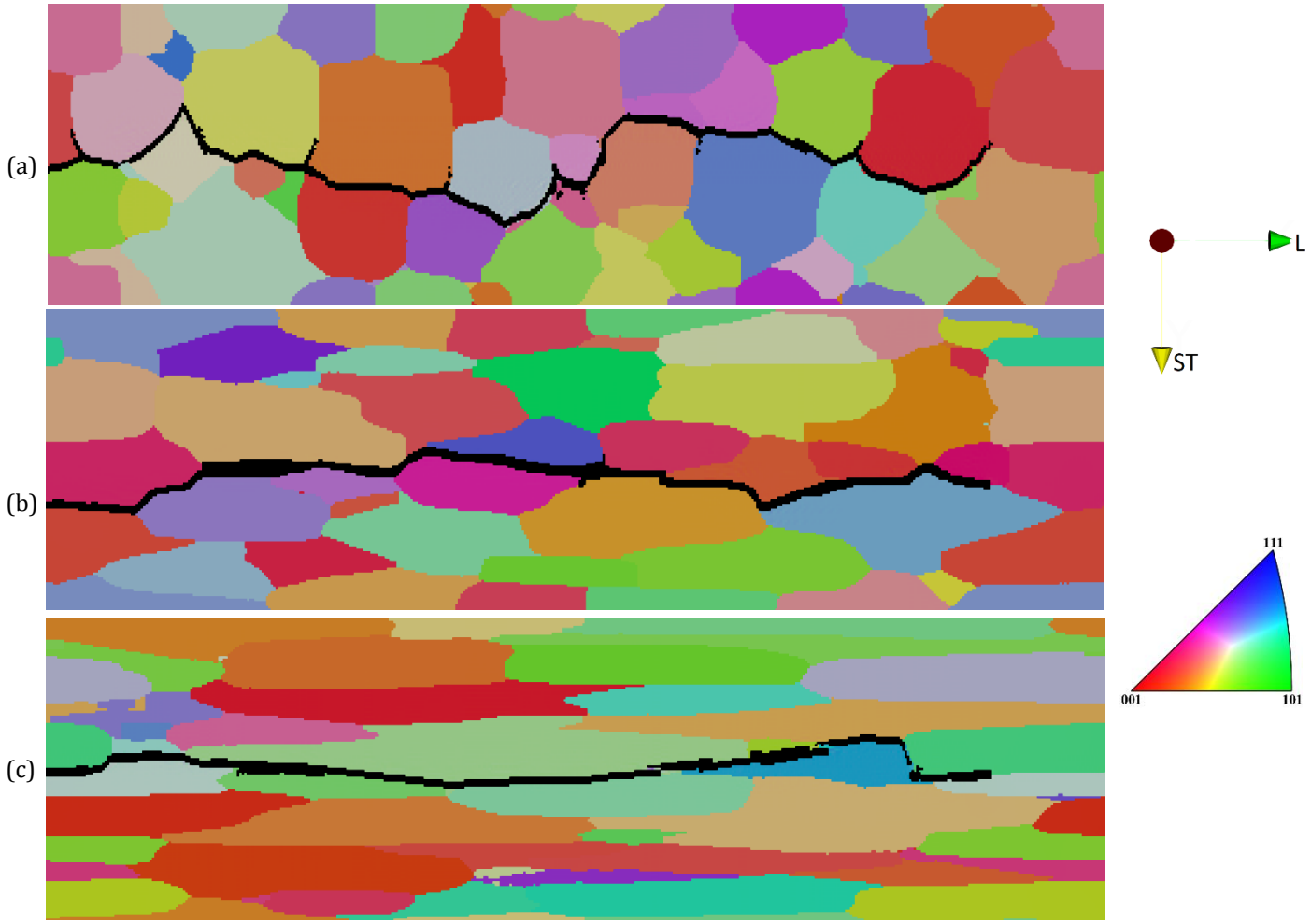

Figure 7: Examples of Crack propagation paths in VE's with simulated grain structures with different grain aspect ratios designed to replicate the typical rolling reductions used on processing thick plates showing the fracture surfaces in 3D and 2D slices through the models' centre L-ST plane; (a) equiaxed unrolled, (b) 50% rolling reduction, (c) 75% rolling reduction.

The higher spatial resolution normalised strain energy release rates obtained from the VE's with different rolling reductions are shown in Figure 8(a) plotted against crack length. In the simulations the average calculated strain energy release rates are again seen to be strongly affected by the overall GB topography, being highest for the most elongated grain case (RR = 75 %), which reflects easier crack propagation, and the lowest driving force was obtained for the equiaxed case. However, there is far more noise in the higher resolution data than seen previously in Figure 3 when a large crack advance increment was used, which averaged over more local events. Overall, the average strain energy release rate values obtained were ~ 30 % lower for the equiaxed grain structure compared to the 75 % rolling reduction case and illustrate a greater ease for crack propagation when there is a more fibrous grain structure. This is a direct consequence of the average geometric grain shape change on increasing the rolling reduction without any recrystallization, which leads to the grain boundaries becoming increasingly elongated and aligned closer to parallel to the rolling plane so that a crack path propagating in the LT-L plane will be able to follow a plane closer to normal to the tensile loading axis. This also means encountering a lower number of grain boundary junctions per unit crack area, where the crack path will also be deflected through a smaller angle. Overall, this results in a smoother fracture surface, as can be seen in Figure 7 and a lower reduction in the average crack driving force relative to the fully planar crack. This contrasts with the equiaxed case, where the crack interacts with a greater number of grain junctions for the same horizontal path length, which also deflect the crack more as the GB faces are more misaligned with respect to the rolling plane. Together, this results in a rougher and more

topographic fracture surface and more strain energy must be released per unit crack extension for the crack to propagate.

It is also noteworthy from Figure 8(a) that increasing the rolling reduction further to 75% has a more limited effect on G_n, than applying the initial rolling reduction of 50%. Overall, this suggests that, without considering the additional effect of partial recrystallization, EAC crack growth rates are expected to be significantly higher in fully unrecrystallised hot rolled plates, than in an equiaxed grain structure, but reducing the plate thickness in the range of 75 – 150 mm has a more limited effect on the average crack driving force.

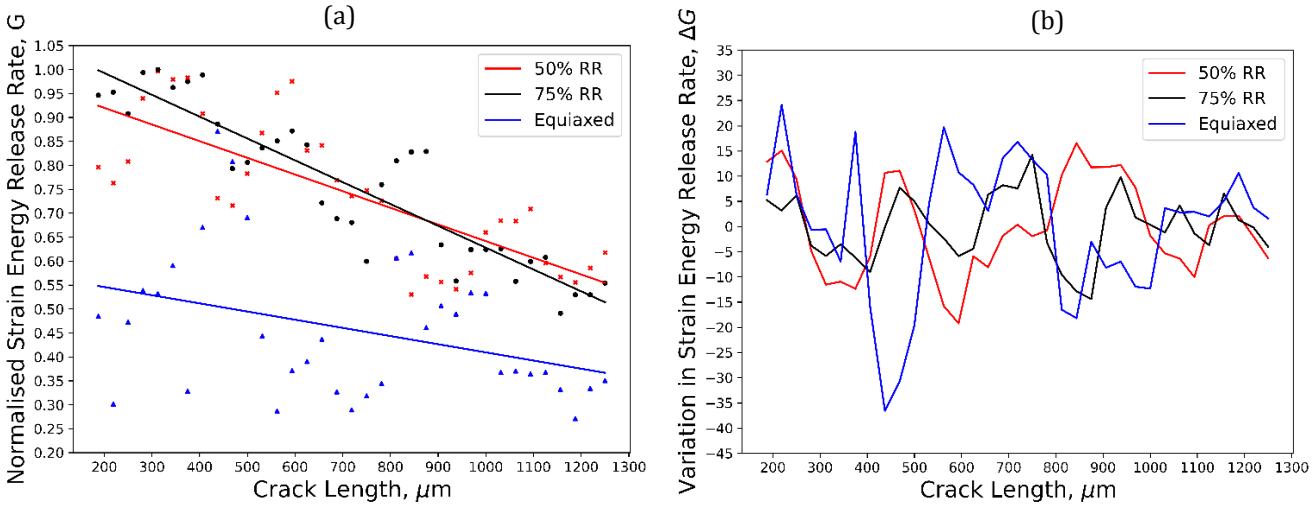

Figure 8: The simulated effect of synthetic unrecrystallised grain structures generated with different rolling reductions (0, 50 and 75%), using a high-resolution crack advance increment of 31 μm plotted against crack length showing; (a) the normalised strain energy release rate, G_n, at each increment, and (b) their local deviation from the linear regression trend line, ΔG_n.

In Figure 8(b), the local variation in the strain energy release rate, ΔG_n, has also been plotted for each increment of crack advance, which was obtained by calculating the deviation from the line of best fit to the data in Figure 8(a). From Fig. 8(b) it can be seen that local events can have a dramatic effect on the crack driving force and that this becomes more extreme with the equiaxed grain structure because of the greater crack deflection angle and deviation distance from a planar path. The crack advancing through the equiaxed grain structure in the L direction encountered a total of 22 grain boundary junctions, which was markedly higher in comparison to the 50% and 75% rolling reduction microstructures, which encountered approximately 11 and 8 respectively. This provides further insight as to why the strain energy release rate results for the rolled microstructures were similar; i.e. because they encountered a relatively similar number of grain boundary junctions. From Figure 8 it can also be seen that local events occur more frequently in the equiaxed grain structure and are more extreme. This can locally reduce the crack driving force by as much as 36% relative to the average trend line. In comparison, local events in the rolled microstructures typically only reduce the crack driving force by ~ 10-20% relative to the average trend line.

Finally, Figure 9 highlights the growth sequence and local change in G_n for the equiaxed plate at a position in the model where a propagating crack encounters a GB junction that significantly deflects the crack, before following around the grain boundary to become more closely aligned with the rolling plane. It can be seen that during this sequence there is a large transient reduction in the mechanical driving force experienced by the model, which then increases again back to the trendline, average, once the highest point of deflection has been passed.

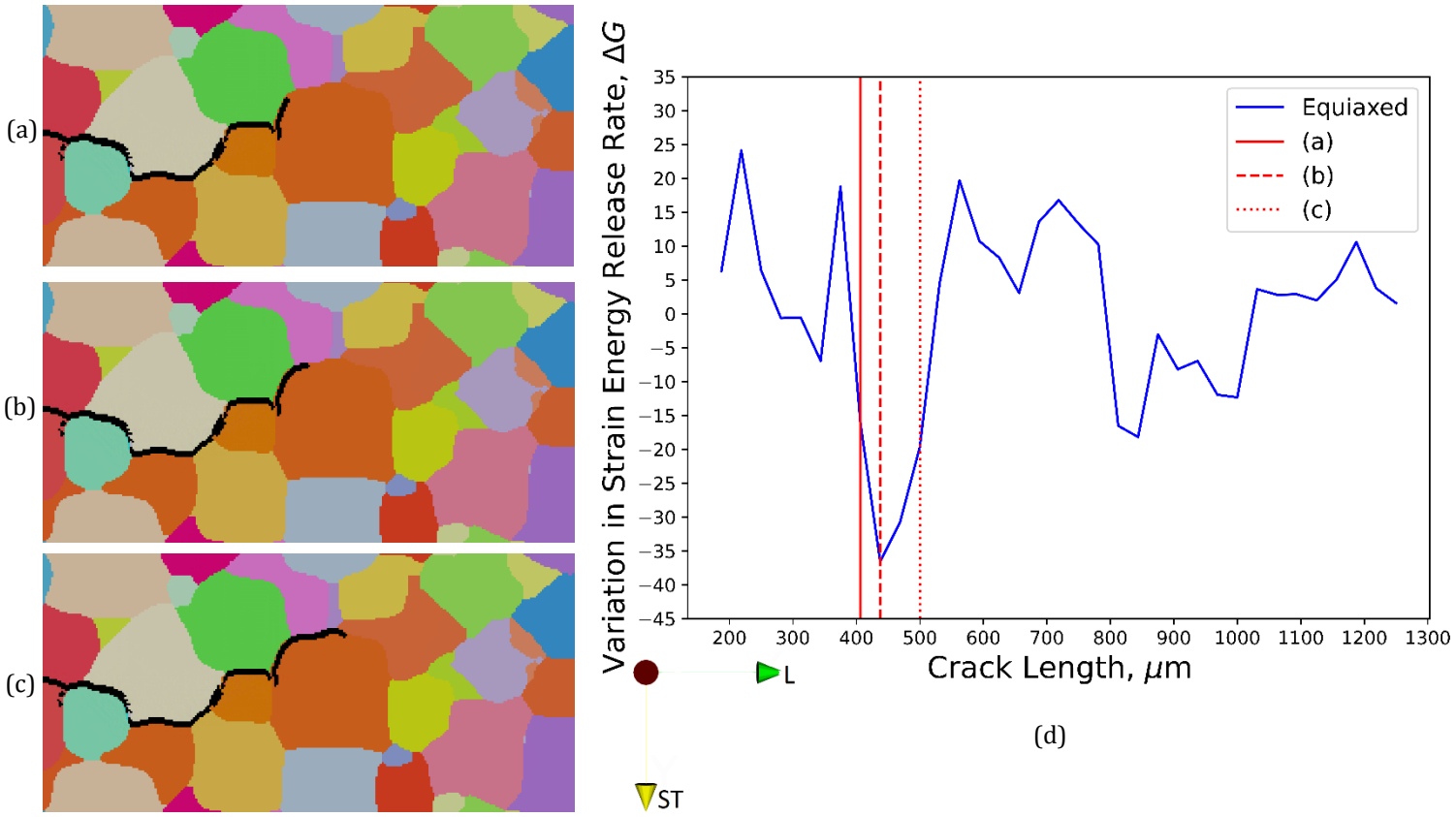

Figure 9: Magnified views highlighting the crack growth sequence (a) – (c) and local change in G (d) in a simulated equiaxed plate at a position in the model where a propagating crack encounters a GB junction that causes significant deflection.

Effect of embedded recrystallised grains

It is difficult to fully avoid partial recrystallisation in rolled 7xxx thick plate alloys due to their high solution treatment temperatures and the heterogeneous distribution of Al_3Zr dispersoid particles that are present in the alloys to inhibit recrystallisation [51]. It is therefore useful to investigate the effects of embedding larger-recrystallised grains in a fibrous grain matrix on the local crack driving force. In alloys such as AA7085, the recrystallized grain volume fraction is typically in the range of 10-20% [39]. When analysed in 3D it has recently been shown that the recrystallized grains can have complex shapes as, due to inverse segregation of Zr, they follow the inter-dendritic regions inherited from the original cast billet [20]. Nevertheless, here a more simplified approach was taken of studying VE's containing single equiaxed 'recrystallised' grains embedded in their centre, in a matrix formed by the standard representation of the AA7085 alloy that contained fibrous 'uncrystallised' grains with a fixed L/ST aspect ratio. To achieve this, an unaltered grain (coloured grey in Figure 10a) was selected in the centre of a standard VE to be used as a baseline data set. Cracks were then grown in three VE's which were kept identical apart from the selected grain, which was progressively increased in size and reduced in aspect ratio (Figures 10 a-d). The cracks were again propagated with a higher-resolution advance increment of 31 μm, and the results compared to the baseline dataset.

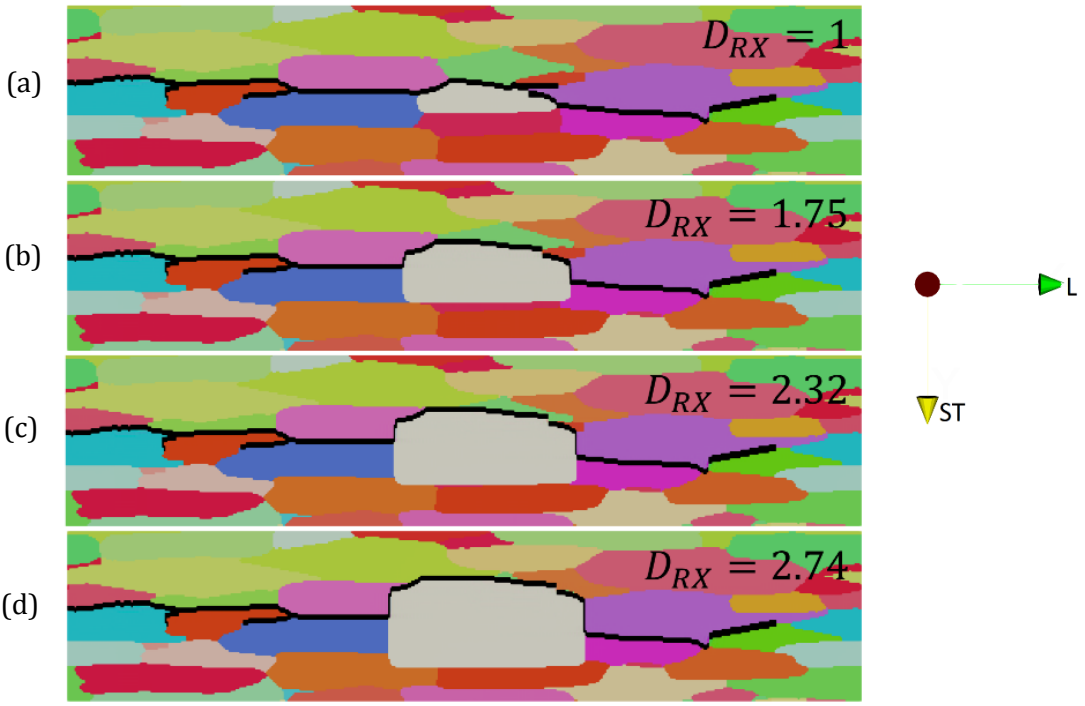

Figure 10: Illustration depicting the effect of the 'growth' of an artificial 'recrystallised' grain on the crack propagation path in a VE with a fibrous matrix grain structure; (a) baseline comparison case, where the recrystallised grain is statistically similar to the other grains in terms of size, and (b), (c) and (d) with a progressively increasing diameter, D_{RX}, and reducing L/ST aspect ratio.

Figure 10 illustrates how when the selected recrystallised grain is grown in volume it influences the crack propagation path. In each model iteration the crack was forced to deviate more around the increasingly large recrystallised grain. Figure 11 reveals how the strain energy release rate was affected in the models as the crack approached and propagated around this grain. As the matrix VE grain structure was held constant, the fracture path was identical in each case except for the local region surrounding the recrystallised grain, where greater crack deflection can be seen as it increased in size. A constant matrix VE grain structure ensures that the calculated strain energy release rate values will be identical for all D_{RX} values prior to the crack front encountering the large recrystallised grain. The strain energy release rate calculations first show a large reduction as the crack is deflected by the recrystallized grain, which becomes greater as its grain size to matrix grain size ratio increases. However, once the crack has passed the recrystallised grain and goes back to propagating in the fibrous matrix grains the energy release rate recovers to follow a similar slope to that shown by the baseline VE. Overall, the effect of the recrystallised grain is a reduction in the strain energy release rate averaged over the whole model of the order of 37% for the largest grain. However, locally at the point of deflection there is a massive decrease in the crack driving force, which even with these simplified geometries was as high as 65%.

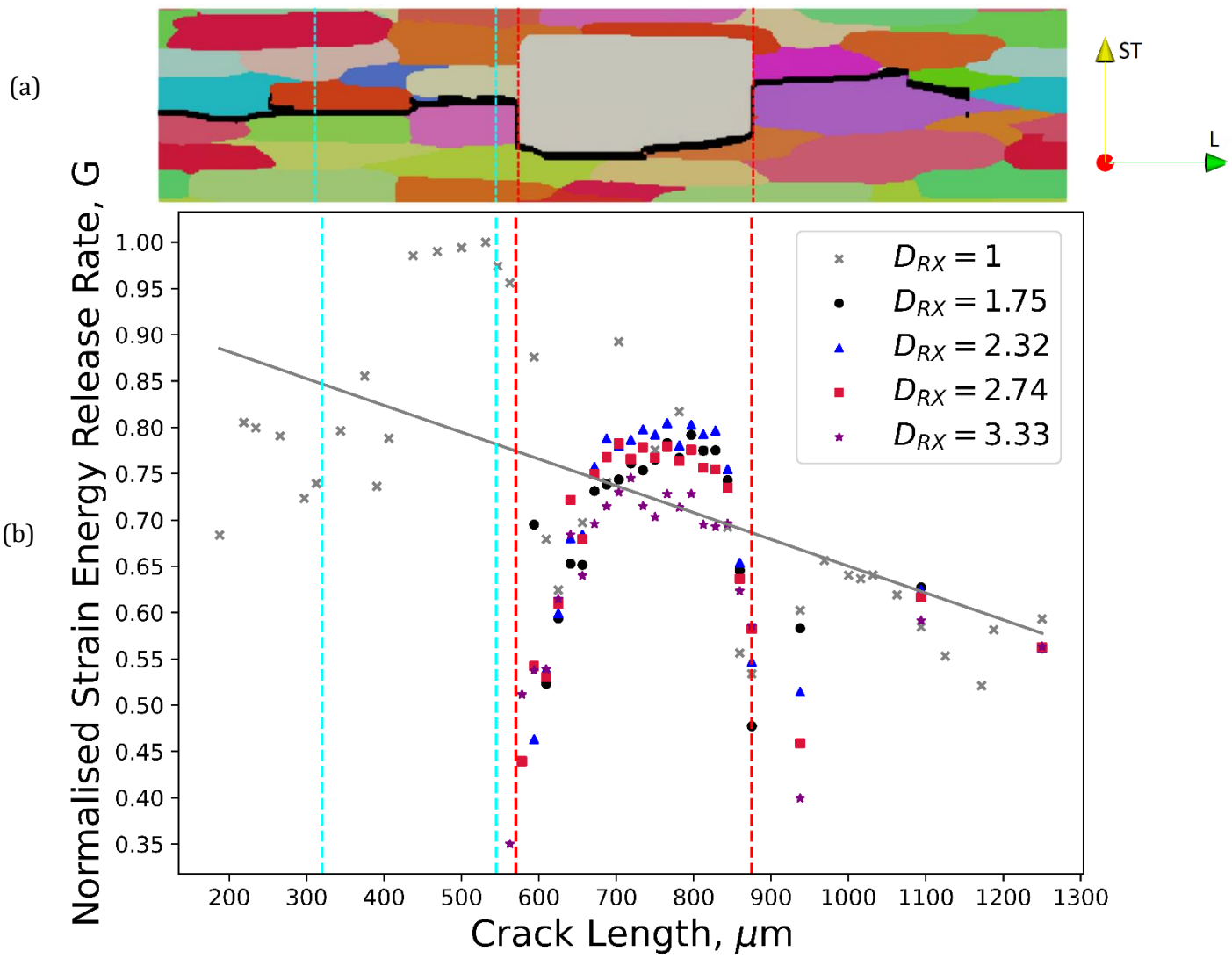

Figure 11: Comparison of the effect of embedding a single recrystallized grain in the centre of the standard grain structure VE with increasing size relative to the matrix (D_{RX}), on the relative strain energy release rate, G_n. The large local drop-in strain energy release rate is indicative of the reluctance a crack to take such a highly deviated propagation path. Larger D_{RX} ratio values can be seen to cause a larger decrease in G.

Since the strength of 7xxx alloys is dominated by precipitation hardening [21], and they are also stretched 2-3% to relieve residual stresses prior to aging, recrystallized gains are not expected to be significantly softer than their surrounding non-recrystallised neighbours. Nevertheless, for other material scenarios it is interesting to understand the extent to which the presence of a softer grain might theoretically impact on the calculated crack driving force. Additional simulations were therefore also performed with a range of relative yield-stress reductions for the recrystallised grain with a D_{RX} value of 2.3. It was discovered that a large reduction in the recrystallised grain yield stress was required to induce a significant drop in the short crack driving forces. This drop in G_n occurs because softer grains store less elastic strain energy prior to plastic deformation. However, an extreme 50% reduction in the yield stress of the recrystallised grain caused only a 2% drop in the calculated average strain energy release rate, which suggests this effect can be ignored in the current context.

4. Discussion of the Significance of the simulations

The focus of this paper is to highlight the substantial influence of grain topography on the local mechanical driving force associated with microstructurally short crack propagation problems, and to help quantify the extent of its variability in partially recrystallized new generation AA7085 thick-plate alloys. Studying the effects of systematically modifying the crack surface topography, crack bifurcation, and deflection, in a realistic synthetic grain structure, has allowed a greater understanding of such effects on the real driving forces for crack propagation, which are often replaced by idealised geometries in fracture mechanics calculations.

4.1 Correlation between G_n and grain topography

The trends discussed above pertaining to the influence of grain topography on the short crack driving forces, are substantiated by several studies. For example, Ricker has used a statistical analytical model to show that in SCC grain structure topography can reduce K_1 by as much as 50% [23]. Yu et al. [55] have also altered the grain size to change the tortuosity of cracks in AA7050 ingots and AA7050-T7651 plates, and showed higher fracture toughness values when the fracture paths were more tortuous. In addition, it has been reported by Warner et al that the effect of rolling reduction on grain aspect ratio can increase crack propagation rates in thinner plates [19]. It is also well known that there is a strong effect of grain direction on EAC propagation in wrought products [44]. It is thus clear that a fracture path with greater topography results in lower overall crack driving force. Such effects are not limited to aluminium alloys and have been more widely studied in the context of the brittle fracture of ceramics [57-59], which it could be argued is comparable to brittle hydrogen-induced crack propagation.

It has also been qualitatively shown that decreasing the grain size increases the resistance to Stress Corrosion Cracking (SCC)[66,67,68], which further aligns with the results presented in this paper. Overall, this work suggests that fibrous elongated grains with high aspect ratios reduces crack path tortuosity, which lowers fracture resistance, and introducing a heterogeneous grain structure can be an important method of deflecting cracks and increasing the fracture resistance of brittle materials.

4.2 Implications for EAC driving forces

In aluminium alloys EAC is a complex dynamic process involving stress-assisted chemical reaction at freshly exposed surfaces, which generates hydrogen by reduction of surface water molecules, or cathodically under immersed conditions [60]. The local stress state at the crack tip is essential to provide the mechanical driving force and to concentrate the hydrogen that is locally absorbed into the material and leads to inter-granular cracking by a combination of hydrogen enhanced decohesion (HEDE) and hydrogen induced local plasticity (HELP), or adsorption induced dislocation emission AIDE) [61]. Long cracks, with larger crack fronts that interact with 100's of grains, will on average exhibit a smooth continuous growth, but will advance intermittently in local burst across their crack front, determined by the local grain structure, boundary resistance, rate of chemical reaction, and effective K [26]. In some instances, this can lead to more significant obstacles like recrystallized grains being bypassed and leaving behind metal ligaments to be torn later as the crack opening displacement increases, which inhibits the crack opening displacement and shields the crack tip [56,62].

The smaller-scale simulations presented within this paper illustrate that for inter-granular EAC there is a strong effect of the purely morphological aspects of microstructure on the overall local mechanical driving force for crack propagation, when described by the elastic strain energy release rate as the crack advances [63]. The results confirm that, in the hot rolled materials simulated, grain topography can substantially lower the volume-averaged driving force for propagation of cracks by approximately 30%, relative to a smooth planar bicrystal crack, or by as much as 50% in a 50% rolled plate if bifurcation is taken into account. For more equiaxed grain structures, estimates from the simulations suggest the volume averaged driving force required for propagation of cracks will be higher and can increase by the order of 50% (without bifurcation). These results in themselves can be important when considering using idealised planar cracks, or simplified crack geometries, in conjunction with linear-elastic fracture mechanics calculations to estimate crack driving forces when comparing lab-test data between different

materials. For example, in for Double Cantilever Beam SCC tests long crack data is frequently expressed as v-K_1 plots with K_1 calculated from the crack length according to ASTM standard G168 [8]. Idealized penny-shaped crack models are also sometimes used to evaluate slow strain rate test data [64], which will not give a full understanding of microstructure influences on the crack driving force. In addition, these simulations show that thermomechanical processing routes that lead to uncrystallised highly fibrous ribbon-like grain structure will be highly determinantal to EAC resistance, if tensile loading is normal to the planar grain boundaries, and should be avoided.

Perhaps more importantly, recently it has been shown by direct in-situ observation that microstructurally short EAC cracks exhibit high levels of scatter, with the growth rate dropping intermittently to near-zero from an upper limit [26,63]. Crack arrest markings (CAMs) on EAC fracture surfaces also provide evidence of the intermittent behaviour of short cracks [65]. However, high strength 7xxx alloys contain local variations in their distributions' of constituent particle and grain boundary precipitates, as well as in their grain boundary orientations and segregation [10]. These factors are important in determining the chemical reactivity of individual grain boundaries and their ability to trap hydrogen, which could enhance decohesion of specific interfaces, as well as influence the mechanical strength of the boundaries [52,61]. The cracking resistance of individual boundaries will therefore vary considerably. Nevertheless, this work has shown that much of the scatter in growth rates of short cracks can still be attributed to the variation in the local crack driving force caused by purely morphological aspects of the grain structure. The strain energy release rate G, varied by as much as 20% in a fibrous grain structure when GB junctions were encountered and the crack deflected on to a new GB plane. This effect also became more severe in less fibrous grain structures due to the larger deflection angles when a triple point was encountered and in an equiaxed microstructure the local driving force on crack-path grain switching was predicted to fall by over 50%. In addition, the simulations have shown that where more heterogeneous grain structure features are encountered, such as embedded recrystallized grains, short cracks can potentially be deflected to such an extent that their driving force becomes so low they will not continue growing and therefore will not transition from initiation to sustained propagation [48].

4.3 Limitations of the presented modelling procedure

While not unique to this modelling technique, the use of a pre-defined crack propagation path could be considered a limitation of the model. This drawback is, however, shared with cohesive zone models, which also require a user-defined crack propagation path [53]. At the final stage of the VE generation process, the crack propagation path was selected to be as realistic as possible, by following the path of highest strain energy release rate. This was achieved by selecting the crack path that deviated least from a plane normal to the applied stress by minimising the deviation produced when the crack encountered new grains.

In addition to aforementioned concerns regarding total VE size, there are currently severe limitations associated with the VE's ability to faithfully reproduce the complex shapes of real-world recrystallised grains. In reality, recrystallised grains are not as simplistic as the ones presented throughout this paper. Garner [40] has presented detailed XCT scans of recrystallised grains found in AA7XXX alloys. The complexity of the surface topology displayed by these 'real-world' recrystallised grains far exceeds that of the grains presented in this study, and can also include re-entrant grain boundaries which will more severely affect crack propagation. For example, Burnett et al [54] have observed cracks that have been forced to form multiple branches when encountering recrystallsied grains, thus lowering the effective crack driving force. This would suggest that more extreme examples have been observed by experimental procedures than the significant path deviations associated with the larger recrystallised grains presented in section 4.4. Despite this, the simpler more spherically-shaped grains presented in this work still provide valuable insight into the extent to which recrystallised grains can have a large influence on the local variation in crack strain energy release rate.

5. Conclusion

A crystal plasticity static-fracture model, that utilised realistic synthetic grain structure VEs, has been applied to estimate the effect of different grain structures on the crack propagation strain energy release rates of microstructurally short cracks in a thick-plate aluminium alloy, AA7085-T7651. In particular, the effect of the grain aspect ratio, related to the rolling reduction, and partially recrystallised grains embedded within a fibrous grain matrix were considered. The modelling work-flow encompassed the generation of synthetic microstructures produced in DREAM.3D, as well as the use of a spectral method analysis in DAMASK. The models were used to simulate the crack propagation behaviour during tensile opening of microstructurally short inter-granular cracks.

Overall, the results illustrate that there is a strong effect of grain boundary topography that can reduce the average crack driving force by as much as 50%, due to a combination of crack path deviation and crack bifurcation. Even though elongated fibrous grains gave a favourable crack path in the rolling plane with less topography than an equiaxed polycrystal microstructure, a large reduction of 30% was still found in the average crack driving force relative to an ideal smooth-planar crack, even without bifurcation.

However, it is shown that on a local scale crack deflection at grain boundary junctions, where the crack switches to a new boundary plane, can lead to even higher temporary reductions in the local crack tip driving force. This behaviour can readily account for the large crack growth rate variability observed for short-cracks and in cases where cracks are more severely deflected by recrystallized grains will prevent embryonic cracks transitioning from initiation to sustained propagation.

Finally, the simulations showed that when cracking occurs in the rolling plane due to out of plane tensile loads, as is normally observed in practice, it would be expected that higher rolling reductions with fully un-recrystallized microstructures will lead to significantly worse EAC performance.

Declaration of Competing Interest

The authors declare that they have no known competing financial interests or personal relationships that could have appeared to influence the work reported in this paper.

Acknowledgements

Professor P.B. Prangnell is grateful to the Royal Academy of Engineering, UK, and Airbus for financial support through the Airbus-University of Manchester Centre for Metallurgical Excellence. The authors are also appreciative of the EPSRC programme grant LightForm (EP/R001715/1) and the Metallic Systems CDT (EP/L016273/1) for supporting aspects of this research, as well as the Henry Royce Institute for Advanced Materials, funded through EPSRC grants EP/R00661X/1, EP/S019367/1, EP/P025021/1 and EP/P025498/1.

References

1. Starke, E.A., Staley, J.T., Application of modern aluminum alloys to aircraft, Prog. Aerospace Sci., 32 (1996), pp. 131-172

2. Williams, J.C., Starke Jr, E.A., Progress in structural materials for aerospace system, Acta Mater., 51 (2003), pp. 5775-5799

3. Gangloff, R.P., Milne, I., Ritchie, R.O., Karihaloo, B., Petit, J., Scott, P., Hydrogen assisted cracking of high strength alloys, Comprehensive Structural Integrity, Vol. 6, Elsevier Sci. New York, NY (2003), pp. 31-101

4. Bucci, R.J., Warren, C.J., Starke Jr., E.A., Need for new materials in aging aircraft structures, J. Aircr. Spacecr. Technol., 37 (2000), pp. 122-129

5. Sarkar, B., Marek, M., Starke Jr., E., The effect of copper content and heat treatment on the stress corrosion characteristics of Al-6Zn-2Mg-X Cu alloys Metall. Trans., 12A (1981), pp. 1939-1943

6. Boselli, J., Wang, W., Weiland, H., Rollett, A.D., Cassada, W.A., The metallurgy of high fracture toughness aluminum-based plate products for aircraft, 13th Int Conf on Al Alloys (ICAA13), Pittsburgh, PA, TMS (2012)

7. A. Association, et al., International alloy designations and chemical composition limits for wrought aluminum and wrought aluminum alloys, Teal Sheets (2018)

8. E. ASTM, G168-17: Standard practice for making and using pre-cracked double beam stress corrosion specimens, West Conshohocken, PA: ASTM Intl (2017).

9. European Aviation Safety Agency, EASA, Environmentally Assisted Cracking in Certain Aluminium Alloys, Safety Information Bulletin 2018–04R1, (2018) https://ad.easa.europa.eu/ad/2018-04R1

10. Holroyd, N.J. H., Burnett, T. L., Lewandowski, J. J., Scamans, G. M., Environment-Induced Cracking of High-Strength Al-Zn-Mg-Cu Aluminum Alloys - Past, Present and Future, CORROSION (2023) 79 (1): 48–71. http://meridian.allenpress.com/corrosion/article-pdf/doi/10.5006/4149/3134719/cj-2206-ir-4149-file001.pdf

11. Djukic, M. B., Bakic, G. M., Zeravcic, V. S., Sedmak, A., Rajicic, B., The synergistic action and interplay of hydrogen embrittlement mechanisms in steels and iron: Localized plasticity and decohesion, Engineering Fracture Mechanics, Volume 216, 2019, 106528, ISSN 0013-7944, https://doi.org/10.1016/j.engfracmech.2019.106528.

12. Holroyd, N.J.H., Scamans, G.M., Crack propagation during sustained-load cracking of Al-Zn- Mg-Cu aluminum alloys exposed to moist air or distilled water, Metall. Mater. Trans. A, 42 (2011), pp. 3979-3998

13. Holroyd, N.J.H., Scamans, G.M., Stress corrosion cracking in Al-Zn-Mg-Cu aluminum alloys in saline environments, Metall. Mater. Trans. A, 44 (2013), pp. 1230-1253

14. Umamahshwer Rao, A.C., Sai Srinadh, K.V., Stress corrosion cracking behaviour of 7xxx aluminum alloys: a literature review, Trans. Nonferrous Met. Soc. China, 26 (2016), pp. 1447- 1471

15. Speidel, M.O., Hyatt, M.V., Fontana, M.G., Staehle, R.W., Stress-corrosion cracking of High-strength aluminum alloys, Advances in Corrosion Science and Technology, vol 2, Springer, Boston, MA (1972), pp. 115-335

16. Speidel, M.O., Stress corrosion cracking of aluminum alloys, Metall. Mater. Trans. A, 6 (1975), pp. 631-651

17. Knight, S., et al, Some effects of alloy composition on stress corrosion cracking in Al–Zn–Mg–Cu alloys, Corros. Sci., 98 (2015), pp. 50-62

18. Knight, S., Lynch, S., et al, Correlations between intergranular stress corrosion cracking, grain- boundary microchemistry, and grain boundary electrochemistry for Al–Zn–Mg–Cu alloys Cor- ros. Sci., 52 (2010), pp. 4073-4080

19. Warner, T., Koschel, D., Whelchel, R., Smith, K. P., Scamans, G., Merrill, R., Effect of testing conditions, gauge and temper on stress corrosion cracking of AA7xxx aluminum aerospace plate alloys, CORROSION 2022; 4142: https://doi.org/10.5006/4142

20. Garner, A., Donoghue, J., Geurts, R., Al Aboura, Y., Winiarski, B., Prangnell, P. B., Burnett, T. L., Large-scale serial sectioning of environmentally assisted cracks in 7xxx Al alloys using femtosecond laser-PFIB,

Materials Characterization, Volume 188, 2022, 111890, ISSN 1044-5803, https://doi.org/10.1016/j.matchar.2022.111890.

21. Ashjari M, Feizi AJ., 7xxx aluminum alloys; strengthening mechanisms and heat treatment: a review. *Material Sci & Eng Int J*. 2018;2(2):49-53. DOI: 10.15406/mseij.2018.02.00034

22. Moody, R., Thompson, A. W., Ricker, R. E., Was, G. W., Jones, R. H., "Hydrogen Effects on Material Behavior and Corrosion Deformation Interactions," TMS (The Minerals, Metals, and Materials Society), Warrendale, PA (2003) pp. 629-638

23. Polak, J., Cyclic Deformation, Crack Initiation, and Low-cycle Fatigue, Academy of Sciences of the Czech Republic, Brno, Czech Republic

24. Jones, R., Peng, D., McMillan, A. J., Chapter Five - Crack Growth From Naturally Occurring Material Discontinuities, Aircraft Sustainment and Repair, Butterworth-Heinemann, 2018, Pages 129-189, ISBN 9780081005408, https://doi.org/10.1016/B978-0-08-100540-8.00005-4.

25. Jones, R., Molent, L., Barter, S., Calculating crack growth from small discontinuities in 7050-T7451 under combat aircraft spectra, Int. J. Fatigue, 55 (2013), pp. 178-182

26. Euesden, R.T., Aboura, Y., Garner, A.J., Jailin, T., Grant, C., Barrett, Z., Engel, C., Shanthraj, P., Holroyd, N.J.H., Prangnell, P.B., Burnett, T.L., In-Situ Observation of Environmentally Assisted Crack Initiation and Short Crack Growth Behaviour of New-Generation 7xxx Series Alloys in Humid Air, Corrosion Science (Accepted - February 2023)

27. J. Mao, Yufei Xu, Dianyin Hu, Xi Liu, Jinchao Pan, Haihe Sun, Rongqiao Wang, Microstructurally short crack growth simulation combining crystal plasticity with extended finite element method, Engineering Fracture Mechanics, Volume 275, 2022, 108786, ISSN 0013-7944, https://doi.org/10.1016/j.engfracmech.2022.108786.

28. Lubich, S., Fischer, C., Schilli, S., Seifert, T., Microstructure-sensitive finite-element analysis of crack-tip opening displacement and crack closure for microstructural short fatigue cracks, International Journal of Fatigue, Volume 162, 2022, 106911, ISSN 0142-1123, https://doi.org/10.1016/j.ijfatigue.2022.106911.

29. Wilson, D., Zheng, Z., Dunne, F.P.E., A microstructure-sensitive driving force for crack growth, Journal of the Mechanics and Physics of Solids, Volume 121, 2018, Pages 147-174, ISSN 0022- 5096, https://doi.org/10.1016/j.jmps.2018.07.005.

30. Shanthraj, P., Eisenlohr, P., Diehl, M., Roters, F., Numerically robust spectral methods for crystal plasticity simulations of heterogeneous materials, International Journal of Plasticity, Volume 66, 2015, Pages 31-45, ISSN 0749-6419, https://doi.org/10.1016/j.ijplas.2014.02.006.

31. Groeber, M.A., Jackson, M.A., DREAM.3D: A Digital Representation Environment for the Analysis of Microstructure in 3D. *Integr Mater Manuf Innov* **3**, 56–72 (2014). https://doi.org/10.1186/2193-9772-3-5

32. De Francisco, U., Larrosa, N. O., Peel, M. J., Hydrogen environmentally assisted cracking during static loading of AA7075 and AA7449, Materials Science and Engineering: A, Volume 772, 2020, 138662, ISSN 0921-5093, https://doi.org/10.1016/j.msea.2019.138662.

33. Diehl, M., Groeber, M., Haase, C. *et al.* Identifying Structure–Property Relationships Through DREAM.3D Representative Volume Elements and DAMASK Crystal Plasticity Simulations: An Integrated Computational Materials Engineering Approach. *JOM* 69, 848–855 (2017). https://doi.org/10.1007/s11837-017-2303-0

34. Roters, F., Diehl, M., Shanthraj, P., Eisenlohr, P., Reuber, C., Wong, S.L., Maiti, T., Ebrahimi, A., Hochrainer, T., Fabritius, H.-O., Nikolov, S., Fri´ak, M., Fujita, N., Grilli, N., Janssens, K.G.F., Jia, N.,

Kok, P.J.J., Ma, D., Meier,F., Werner, E., Stricker, M., Weygand, D., Raabe, D., DAMASK – The Düsseldorf Advanced Material Simulation Kit for modelling multi-physics crystal plasticity, thermal, and damage phenomena from the single crystal up to the component scale, Computational Materials Science, Volume 158, 2019, Pages 420-478, ISSN 0927-0256, https://doi.org/10.1016/j.commatsci.2018.04.030

35. Hutchinson, J. W., Bounds and self-consistent estimates for creep of polycrystalline materials, Proc. R. Soc. A: Math., Phys. Eng. Sci. 348 (1652) (1976) 101–127, https://doi.org/10.1098/rspa.1976.0027.

36. Kalidindi S. R., Incorporation of deformation twinning in crystal plasticity models, Journal of the Mechanics and Physics of Solids, Volume 46, Issue 2, 1998, Pages 267-290, ISSN 0022-5096, https://doi.org/10.1016 S0022-5096(97)00051-3.

37. Khadyko, M., Dumoulin, S., Børvik, T., Hopperstad, O., An experimental–numerical method to determine the work-hardening of anisotropic ductile materials at large strains. International Journal of Mechanical Sciences 88 (2014) 25–36. https://doi.org/10.1016/j.ijmecsci.2014.07.001

38. Maiti, T., Eisenlohr, P., Fourier-based spectral method solution to finite strain crystal plasticity with free surfaces, Scripta Materialia, Volume 145, 2018, Pages 37-40, ISSN 1359-6462, https://doi.org/10.1016/j.scriptamat.2017.09.047.

39. Schwarzenbock, E., Ollivier, E., Garner, A., Cassell, A., Hack, T., Barrett, Z., Engel, C., Burnett, T., Holroyd, N., Robson, J. and Prangnell, P., 2020. Environmental cracking performance of new generation thick plate 7000-T7x series alloys in humid air. Corrosion Science,171, p.108701.

40. Trimby, P., Anderson, I., Larsen, K., Hjelmstad, M., Thomsen, K., & Mehnert, K. (2020). Advanced Classification of Microstructures in EBSD Datasets Using AZtecCrystal. *Microscopy and Microanalysis, 26*(S2), 112-113. doi:10.1017/S1431927620013410

41. Tao Liu, Haitao Jiang, Hui Sun, Yujie Wang, Qing Dong, Jianrong Zeng, Fenggang Bian, Jiao Zhang, Fei Chen, Baode Sun, Effects of rolling deformation on precipitation behavior and mechanical properties of Al–Zn–Mg–Cu alloy, Materials Science and Engineering: A, Volume 847, 2022, 143342, ISSN 0921-5093, https://doi.org/10.1016/j.msea.2022.143342.

42. Mi, Y., Aliabadi, M.H., Three-dimensional crack growth simulation using BEM, Computers & Structures, Volume 52, Issue 5, 1994, Pages 871-878, ISSN 0045-7949, https://doi.org/10.1016/0045-7949(94)90072-8.

43. Wu, Jian-Ying & Nguyen, Vinh Phu & Thanh Nguyen, Chi & Sutula, Danas & Bordas, Stéphane & Sinaie, Sina. (2019). Phase field modelling of fracture. Advances in Applied Mechanics. 53. 1-183, https://www.sciencedirect.com/science/article/pii/S0065215619300134.

44. Holroyd, N.J.H., Environment-induced cracking of high-strength aluminum alloys, Environ. Crack. Met. (1990) 311

45. Gudla, V. C., Storm, M., Palmer, B. C., Lewandowski, J. J., Withers, P. J., Holroyd, N.J.H., Burnett, T. L., Environmentally induced crack (EIC) initiation, propagation, and failure: A 3D in-situ time-lapse study of AA5083 H131, Corrosion Science, Volume 174, 2020, 108834, ISSN 0010-938X, https://doi.org/10.1016/j.corsci.2020.108834.

46. Anderson, T.L. (2017). Fracture Mechanics: Fundamentals and Applications, Fourth Edition (4th ed.). CRC Press. https://doi.org/10.1201/9781315370293

47. Hashiguchi, K., Nonlinear Continuum Mechanics For Finite Elasticity-Plasticity, ISBN: 978-0-12-819428-7

48. De Francisco, U., Larrosa, N. O., Peel, M. J., Hydrogen environmentally assisted cracking during static loading of AA7075 and AA7449, Materials Science and Engineering: A, Volume 772, 2020, 138662, ISSN 0921-5093, https://doi.org/10.1016/j.msea.2019.138662.

49. Robson, J.D., Prangnell, P.B., Dispersoid precipitation and process modelling in zirconium containing commercial aluminium alloys, Acta Materialia, Volume 49, Issue 4, 2001, Pages 599-613, ISSN 1359-6454, https://doi.org/10.1016/S1359-6454(00)00351-7.

50. Jiang, J., Liu, Y.,Xiao, G., Wang, Y., Ju, Y., Effect of pass reduction on microstructure, mechanical properties and texture of hot-rolled 7075 alloy, Materials Characterization, Volume 147, 2019, Pages 324-339, ISSN 1044-5803, https://doi.org/10.1016/j.matchar.2018.11.015.

51. Morere, B., Shahani, R., Maurice, C. *et al.* The influence of Al_3Zr dispersoids on the recrystallization of hot-deformed AA 7010 alloys. *Metall Mater Trans A* **32**, 625–632 (2001). https://doi.org/10.1007/s11661-001-0079-9

52. Wen, M., Li, Z. and Barnoush, A. (2013), Atomistic Study of Hydrogen Effect on Dislocation Nucleation at Crack Tip. Adv. Eng. Mater., 15: 1146-1151. https://doi.org/10.1002/adem.201300123

53. Elices, M., Guinea, G.V., Gomez, J., Planas, J., The cohesive zone model: advantages, limitations and challenges, Engineering Fracture Mechanics, Volume 69, Issue 2, 2002, Pages 137-163, ISSN 0013-7944, https://doi.org/10.1016/S0013-7944(01)00083-2.

54. Burnett, T. L., Holroyd, N.J.H., Scamans, G. M., Zhou, X., Thompson, G. E. and Withers, P. J.. "The role of crack branching in stress corrosion cracking of aluminium alloys" Corrosion Reviews, vol. 33, no. 6, 2015, pp. 443-454. https://doi.org/10.1515/corrrev-2015-0050

55. Yu, F.; Wang, X.; Huang, T.; Chao, D. Effect of Grain Refiner on Fracture Toughness of 7050 Ingot and Plate. Materials 2021, 14, 6705. https://doi.org/10.3390/ma14216705

56. Marrow, T.J., Babout, L., Connolly, B.J., Engelberg, D.L., Johnson, G., Buffiere, J.Y., Withers, P.J., Newman, R.C., High-resolution, in-situ, tomographic observations of stress corrosion cracking, In host publication (2007) 439-447

57. Kleebe, H.-J., Pezzotti, G. and Ziegler, G. (1999), Microstructure and Fracture Toughness of Si3N4 Ceramics: Combined Roles of Grain Morphology and Secondary Phase Chemistry. Journal of the American Ceramic Society, 82: 1857-1867. https://doi.org/10.1111/j.1151-2916.1999.tb02009.x

58. Lee, S.-G., Kim, Y.-W. and Mitomo, M. (2001), Relationship between Microstructure and Fracture Toughness of Toughened Silicon Carbide Ceramics. Journal of the American Ceramic Society, 84: 1347-1353. https://doi.org/10.1111/j.1151 2916.2001.tb00840.x

59. Krstic, Z., Yu, Z. & Krstic, V.D. Effect of grain width and aspect ratio on mechanical properties of Si3N4 ceramics. J Mater Sci 42, 5431–5436 (2007). https://doi.org/10.1007/s10853-006-0826-9

60. McMahon, M.E., Steiner, P.J., Lass, A.B., Burns J.T.; The Effect of Loading Orientation on the Stress Corrosion Cracking of Al-Mg Alloys. CORROSION 1 June 2017; 73 (6): 713–723. doi: https://doi.org/10.5006/2343

61. Lynch, S.P. "Progress Towards Understanding Mechanisms Of Hydrogen Embrittlement And Stress Corrosion Cracking." Paper presented at the CORROSION 2007, Nashville, Tennessee, March 2007.

62. Marrow, T.J., Babout, L., Jivkov, A.P., Wood, P., Engelberg, D.L., Stevens, N., Withers, P.J., Newman, R.C., Three dimensional observations and modelling of intergranular stress corrosion cracking in austenitic stainless steel, J. Nucl. Mater. 352 (2006) 62-74

63. De Francisco, U., Beckmann, F., Moosmann, J. *et al.* 3D characterisation of hydrogen environmentally assisted cracking during static loading of AA7449-T7651. *Int J Fract* 232, 93–116 (2021). https://doi.org/10.1007/s10704-021-00595-y

64. Duffe, T., Kullmer, G., Tews, K., Aubel, T., Meschut, G., Global energy release rate of small penny-shaped cracks in hyperelastic materials under general stress conditions, Theoretical and Applied Fracture Mechanics, Volume 121, 2022, 103461, ISSN 0167-8442, https://doi.org/10.1016/j.tafmec.2022.103461.

65. Aboura, Y., Garner, A.J., Euesden, R., Barrett, Z., Engel, C., Holroyd, N.J.H., Prangnell, P.B., Burnett, T.L., Understanding the environmentally assisted cracking (EAC) initiation and propagation of new generation 7xxx alloys using slow strain rate testing, Corrosion Science, Volume 199, 2022, 110161, ISSN 0010-938X, https://doi.org/10.1016/j.corsci.2022.110161.

66. Jin Qin, Zhi Li, Ming-yang Ma, Dan-qing Yi, Bin Wang, Diversity of intergranular corrosion and stress corrosion cracking for 5083 Al alloy with different grain sizes, Transactions of Nonferrous Metals Society of China, Volume 32, Issue 3,2022, Pages 765-777, ISSN 1003-6326, https://doi.org/10.1016/S1003-6326(22)65831-X.

67. Tang, J., Zhang, Y., Ye, L., Qu, M., Wu, J., Zhang, Z., Liu, S., and Deng, Y., *Effect of Grain Boundary and Crystallographic Orientation on the Stress Corrosion Behavior of an Al-Zn-Mg Alloy*. United States: N. p., 2019. Web. doi:10.1007/S11665-019-04050-X.

68. T.C. Tsai, T.H. Chuang, Role of grain size on the stress corrosion cracking of 7475 aluminum alloys, Materials Science and Engineering: A, Volume 225, Issues 1–2, 1997, Pages 135-144, ISSN 0921-5093, https://doi.org/10.1016/S0921-5093(96)10840-6.

69. Xiaohui Tu, Ahmad Shahba, Jinlei Shen, Somnath Ghosh, Microstructure and property based statistically equivalent RVEs for polycrystalline-polyphase aluminum alloys, International Journal of Plasticity, Volume 115, 2019, Pages 268-292, ISSN 0749-6419, https://doi.org/10.1016/j.ijplas.2018.12.002.

Reviewer #1: This article describes a computational study on the crack growth driving forces in AA7XXX series alloys. A crystal plasticity model is employed and different representative volume elements (RVEs) are simulated in the DAMASK software. The work will be of interest to Materialia readers, and this reviewer recommends the manuscript for publication after the comments below are addressed.

* No affiliations listed for the authors.

This has been addressed

* End of Section 2.2: The variable G is mentioned before it is introduced. Please define G here.

Sorry, this is a mistake from a previous draft and has been fixed

* Section 2.4: Table 2 should refer to Table 1?

This has been corrected

* Is the last page of the submission pdf the graphical abstract? If so, this should be improved with labels of what is displayed. Right now, it is difficult to interpret and not useful to perspective readers.

This has been improved as recommended with additional labels and larger fonts.

* How/why were the crack length bounds of 300 microns to just over 1200 microns decided, as shown in Fig. 3?

This has now been addressed in section 2.3, which now reads: “The minimum simulated crack length was chosen to be 200 µm, as the crack length is similar to the size of the microstructural features that we’re investigating. To investigate crack sizes smaller than this, the cracks would be too heavily influenced by other microstructural features that are not included in the model, such as regions of high dislocation density, precipitates, or pores. Regarding the maximum length, experimental evidence suggests that short cracks begin to transition to long cracks at about the 1 mm mark, as shown by Euesden et al [26]. In addition to this, the overall size of the VE’s impacts computational performance, placing a further upper limit on the crack lengths.” Thus the size range chosen allowed us to effectively investigate the influence on the grain structure on the geometry without unnecessary computing overheads.

* In Fig. 11, why is there only data for D_rx = 1 below ~550 microns?

The text has been updated to make the reasoning behind this clearer, just below Figure 10. Essentially, a constant matrix RVE grain structure ensures that the crack path and local grain structure around the recrystallised grain is the same in each case, meaning that the strain energy release rate values will be the same in the region before the crack meets the recrystallised grain. The text now reads: “As the matrix VE grain structure was held constant, the fracture path was identical in each case except for the local region surrounding the recrystallised grain, where greater crack deflection can be seen as it increased in size. A constant matrix VE grain structure ensures that the calculated strain energy release rate values will be identical for all D_{RX} values prior to the crack front encountering the large recrystallised grain.”

* Section headers in the discussion section are labeled as 5.1, 5.2, etc. but should be 4.1, 4.2, etc.

This has been fixed, thanks for pointing this out.

Reviewer #2: This manuscript mainly investigated the effect of various morphological parameters of microstructure associated with Aluminum alloy AA7085-T7651 on the inter-granular EAC crack propagation utilizing crystal plasticity static-fracture model.
Overall, the work presents some results that could contribute to better understand the EAC crack propagation in AA7085-T7651. Some comments are given as follows:

1. It is stated the RVEs are statistically representative. However, it is unclear about which features the authors are referring to with respect to the real microstructure. The authors should specify the microstructual parameters, e.g., crystallographic or morphological distributions since there are a number of features can be extracted from EBSD data. Also, the 3D RVE created by DREAM3D should be plotted, and the data that shows statistically representation of real microstructure should be given. A good reference could be Fig. 7 in paper by Tu, Shahba, Shen, Ghosh IJP (2019).

1.1 Additional information very similar to the figure cited by the reviewer has been added to the supplementary information. It contains the statistical distribution plots used by DREAM3D to produce the synthetic grain structures, and shows their convergence with the distributions obtained from the real EBSD map. One aspect of this paper is about systematically varying the grain aspect ratio for different RVE's, which makes it difficult to produce an identical figure to the one cited by the reviewer.

Also, the RVEs have the size of 100 grains in this paper. Based on the convergence study by the same reference, it shows that at least 150 grains are needed for microstructural RVE, and 300 grains are required so that the local stress values are converged, which is especially critical for crack propagation. The insufficient number of grains could lead to much different energy release rates of three RVE as plotted in Figure 3. It is suggested the authors should look into this and justify.

1.2. We agree that the convergence study cited by the reviewer is relevant, and that the volume elements used within the study are non-representative, as they do not produce converged average quantities of interest (stress, strain energy release rate, etc). We have modified the manuscript accordingly, where we now refer only to 'Volume Elements', instead of 'Representative Volume Elements'. We have also added Tu, Shahba, Shen, Ghosh IJP (2019) to the list of references in the manuscript. To address the issue of non-convergence of the strain energy release rates, we have simulated several volume elements to quantify the uncertainty range associated with the strain energy release rates. We then only discuss trends in our results that are significantly outside the range of statistical uncertainty associated with the non-converged strain energy release rate values. This ensures that despite not having fully converged average stress values, the results are still valid and meaningful.

2. A figure showing the CP model with boundary condition and loading profile with preexisting crack tip is suggested to add in the section Model Setup for better understanding.

2. This figure for the baseline/planar grain boundary RVE has been added to the supplementary information, which should also resolve comment #11

3. It is known the precipitates could affect the mechanical properties, also failure mode of Al alloy. But this seems not considered in this paper for the microstuctural crack propagation. The author should justify without including it in this study.

3. Precipitates do indeed play a very important role for modelling microstructurally short crack propagation, particularly for EAC cracking. However, this paper is purely trying to isolate how important the morphology of the local grain structure is on the driving forces for short cracks in a cracking process that is purely brittle inter-granular, which is the case with H-embrittlement in EAC

of high Zn 7xxx alloys [Garner et al [20]]. Grain boundary precipitates, although important in determining that the crack path is intergranular, do not control the crack path when it is purely intergranular and are very thin < 100 nm relative to the large grain size, so they have not been considered in this study which focuses purely on the effect of grain topography on the mechanical driving force. It is also very computationally difficult to consider small < 1 µm precipitates at the same time as large grains (>200 µm) in an RVE that includes as statistically reasonable number of grains. For these reasons small precipitates have not been included in the model which purely focuses on large scale grain topography effects. This paper therefore purely focusing focuses on the effect of grain morphology specifically. This is because recent studies (DOI: 10.1016/S1003-6326(22)65831-X, and https://doi.org/10.1007/s11665-019-04050-x) have suggested it was a very important aspect of defining overall EAC performance.

4. Are the material parameters in Table 1 calibrated or taken from literature? What are the parameters are actually calibrated in section 2.4? It is suggested to put Table 1 in Section 2.4 as well if some parameters are calibrated in the paper.

4. The text has been updated to make this a bit clearer, and the changes have been made at the beginning of section 2.4, which now reads: “The aluminium plasticity parameters shown in Table 1 were then slightly adjusted until convergence with the experimental stress-strain data was achieved.” … and... “The material parameters shown in Table 1 for the dilatational air layer were taken from Maiti et al[38].”

5. The Table 2 is confusing. It is saying they are grain statistical parameters, but only grain size distribution is listed. Also, what are the meaning of mu and sigma? The other parameters such as bin step size are merely setting of histogram in DREAM3D, and they are not related to statistical parameters. Please clarify ad correct.

5. We agree this is an oversight. The caption and the title of Table 2 has been amended, and explanations of mu and sigma have been added. Table 2 contains the parameters used to generate the necessary statistics that describe the VE grain structure. The text has been amended to better convey the meaning of the parameters found in Table 2, in accordance with the DREAM3D documentation.

6. While it is good to know the effect of grain morphology on the crack propagation, how about the effect of crystallographic orientations?

6. The effects of the crystallographic orientations are accounted for in the model via the chosen crystal plasticity model, meaning these effects are incorporated/wrapped up into the calculated G value. However, we have not explicitly studied the effects of texture in this paper because these thick plate materials are weakly textured, and so it was deemed to be out with the scope of this paper. This point has been added to in the experimental section 2.2, where it sates; “the texture of thick rolled 7085 plates consist of weak rolling and cube recrystallization components with a maximum intensity of < 3 MRD and was therefore not varied in this study.”

7. Although the simulation results seems correct theoretically, is there any supporting from experimental observations?

7. We have referred to other studies, including model predictions, on the strong effect of grain topography on the mechanical driving force for cracking in the discussion (please see refs [19, 22,60, 63, 65], although few of these are quantitative, which was the motivation for producing this

paper. We have also now added several new qualitative references on the effect of grain size and structure on the susceptibility to SCC and EAC [66, 67, 68]. An additional sentence mentioning these newly added references has been placed in section 4.1.

8. In table 1, the parameter reference slip rate should use the same symbol as given in line 29 equation for Lp

8. The equation for the plastic velocity tensor (Lp) given on line 29 contains a shear contribution for each individual slip plane, $\dot{\gamma}^{\alpha}$, and two unit vectors, s^{α} and n^{α}, which point along the slip direction and slip plane normal, respectively. None of these quantities appear in Table 1, and should therefore not share the same symbols as the slip or slip rate quantities.

9. In Table 1, the asymptotically saturation g is same as initial g0? If so, then there will be no hardening effect. Please check and correct.

9. Thanks for noticing this mistake, the correct g0 value has been added to the table.

10. In line 58, the parameters should be referring to those in Table 1, rather Table 2.

10. This has been corrected

11. What and where is the bicrystal baseline RVE?

11. Please see comment 2

Figure

Click here to access/download;Figure;Figure 1.png

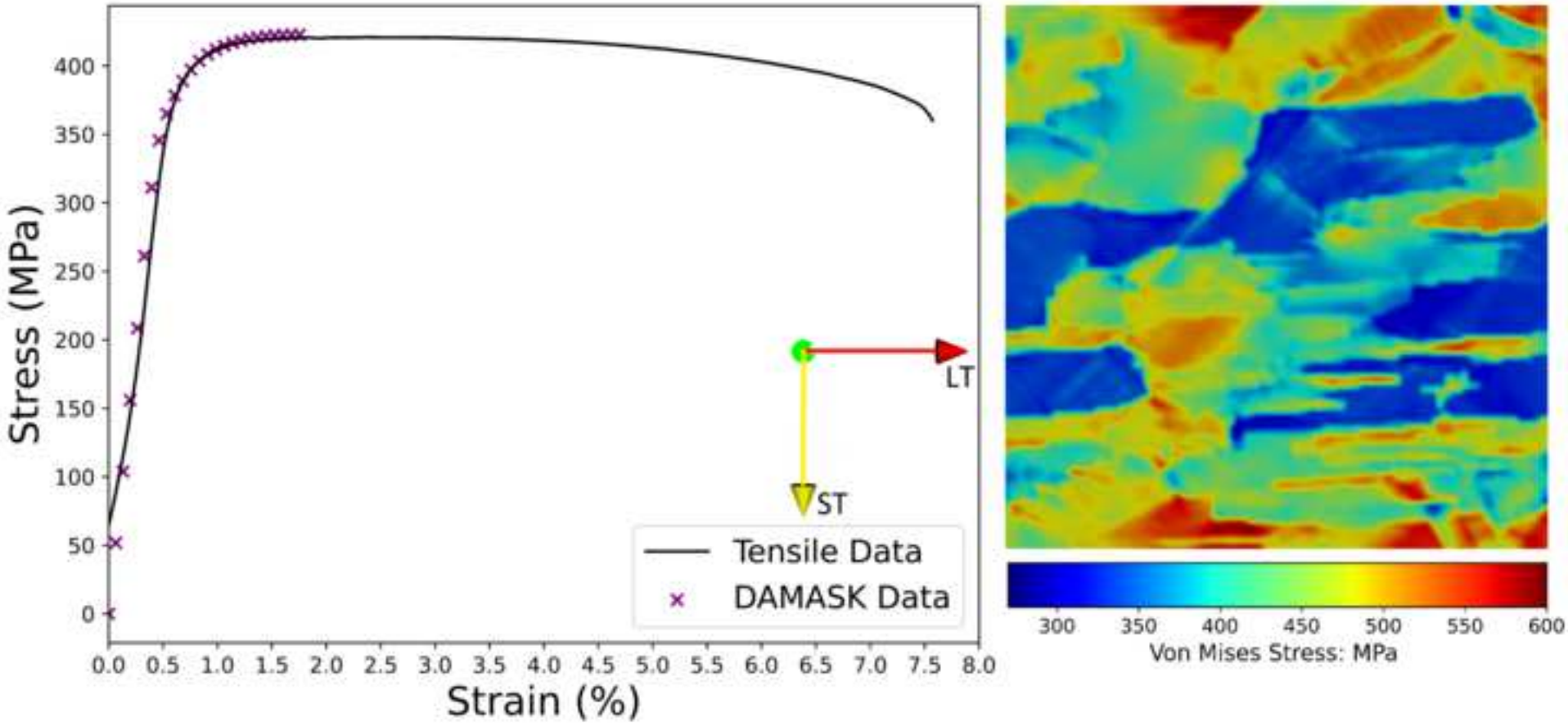

Figure

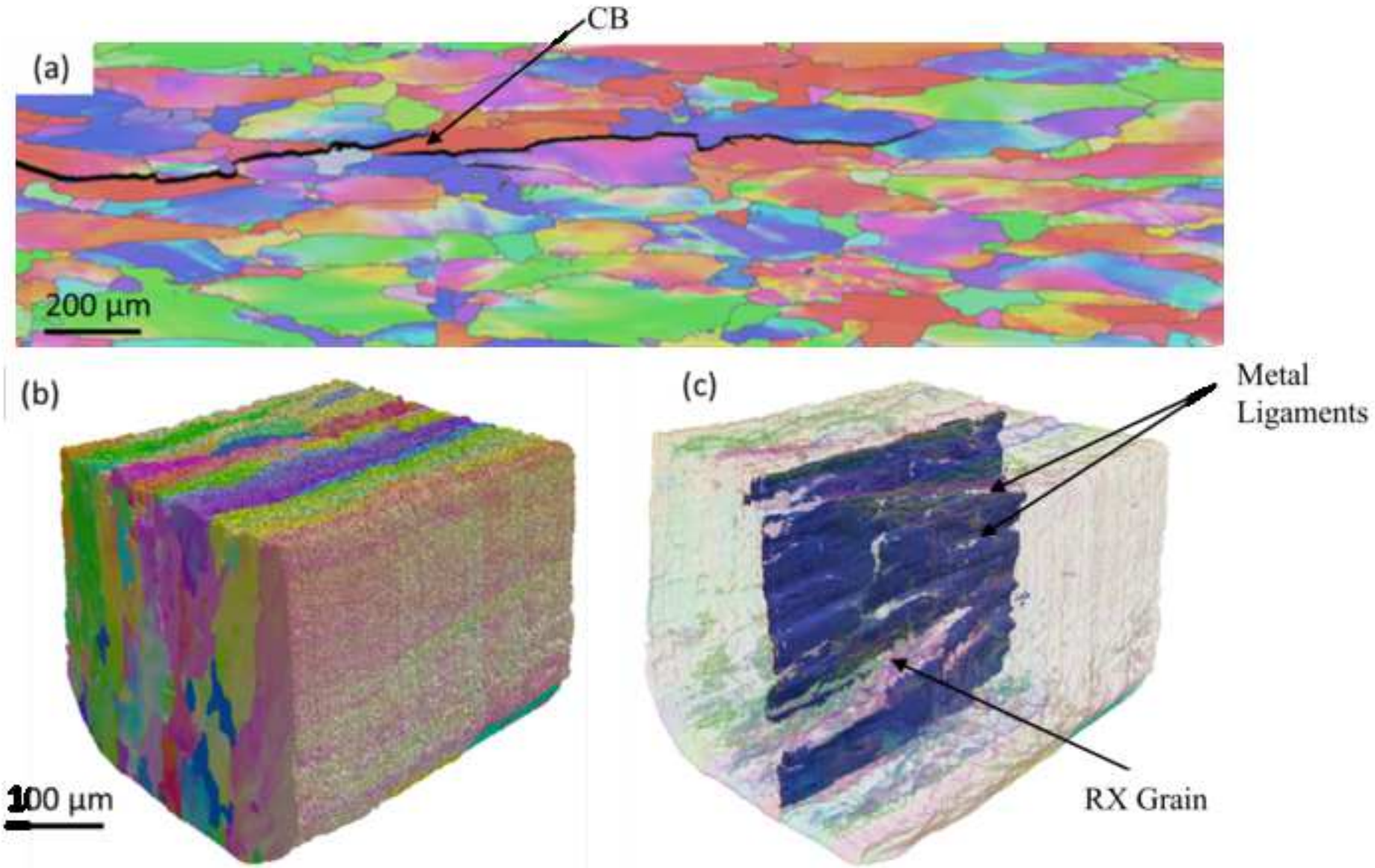

Figure

Click here to access/download;Figure;Figure 3.png

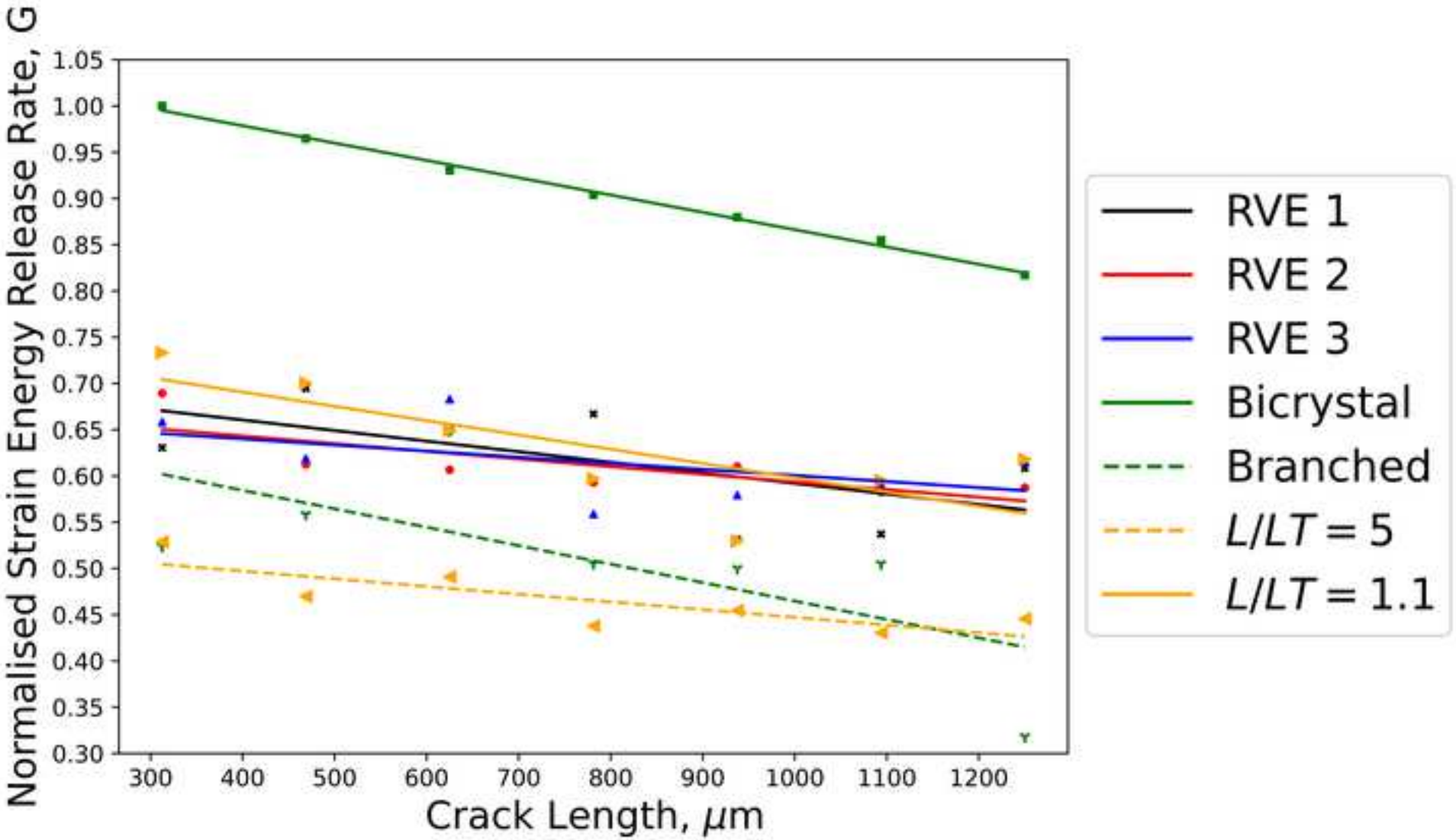

Figure

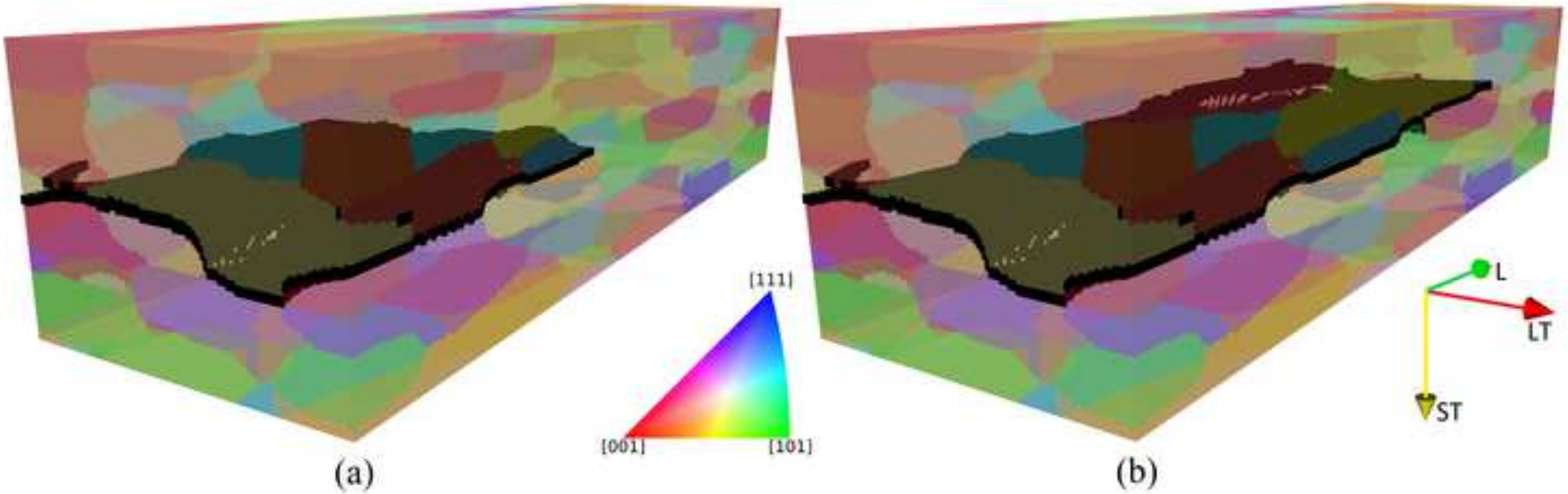

(a) (b)

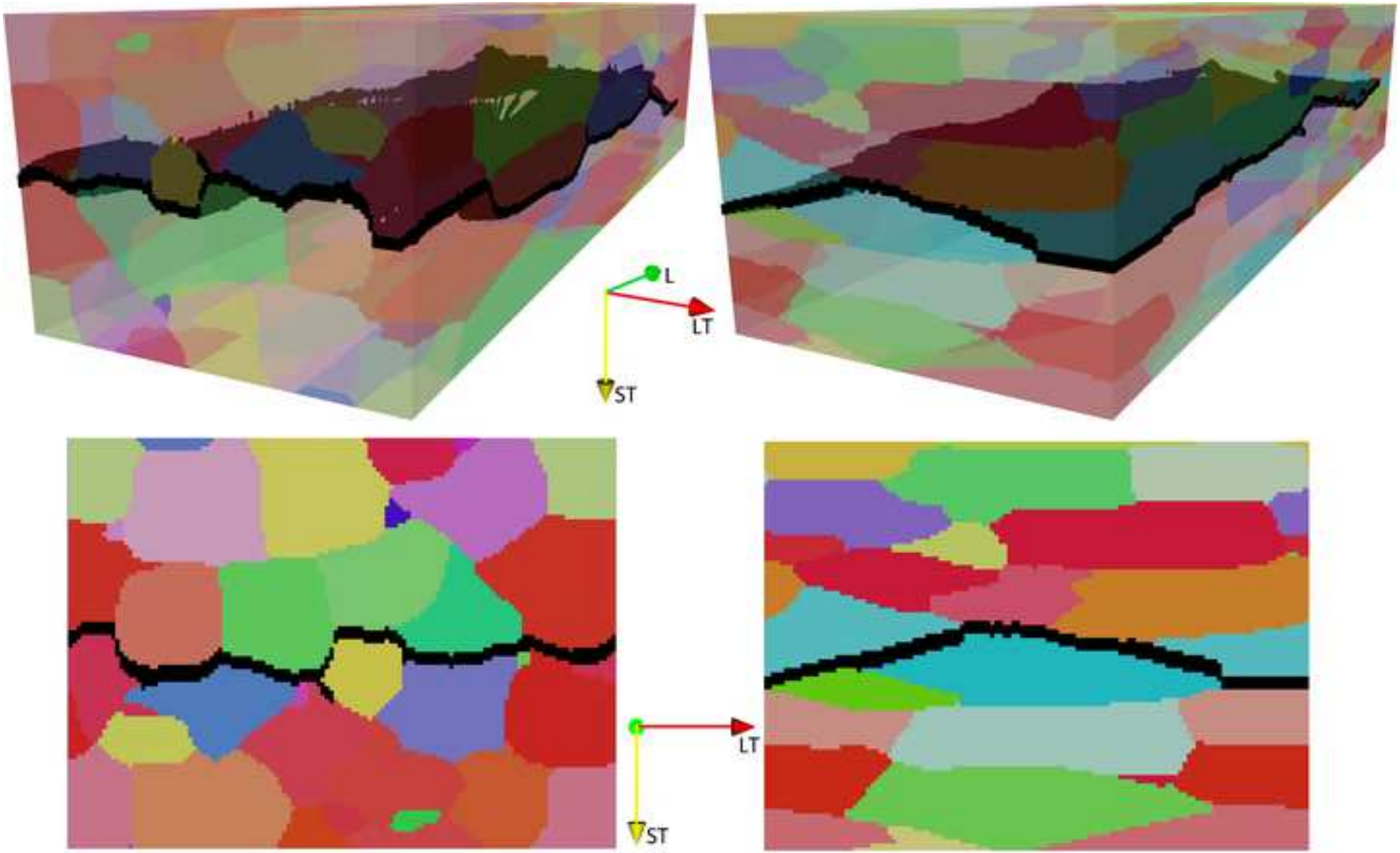

(a) L/LT=5

(b) L/LT = 1.1

Figure

Click here to access/download;Figure;Figure 6.png

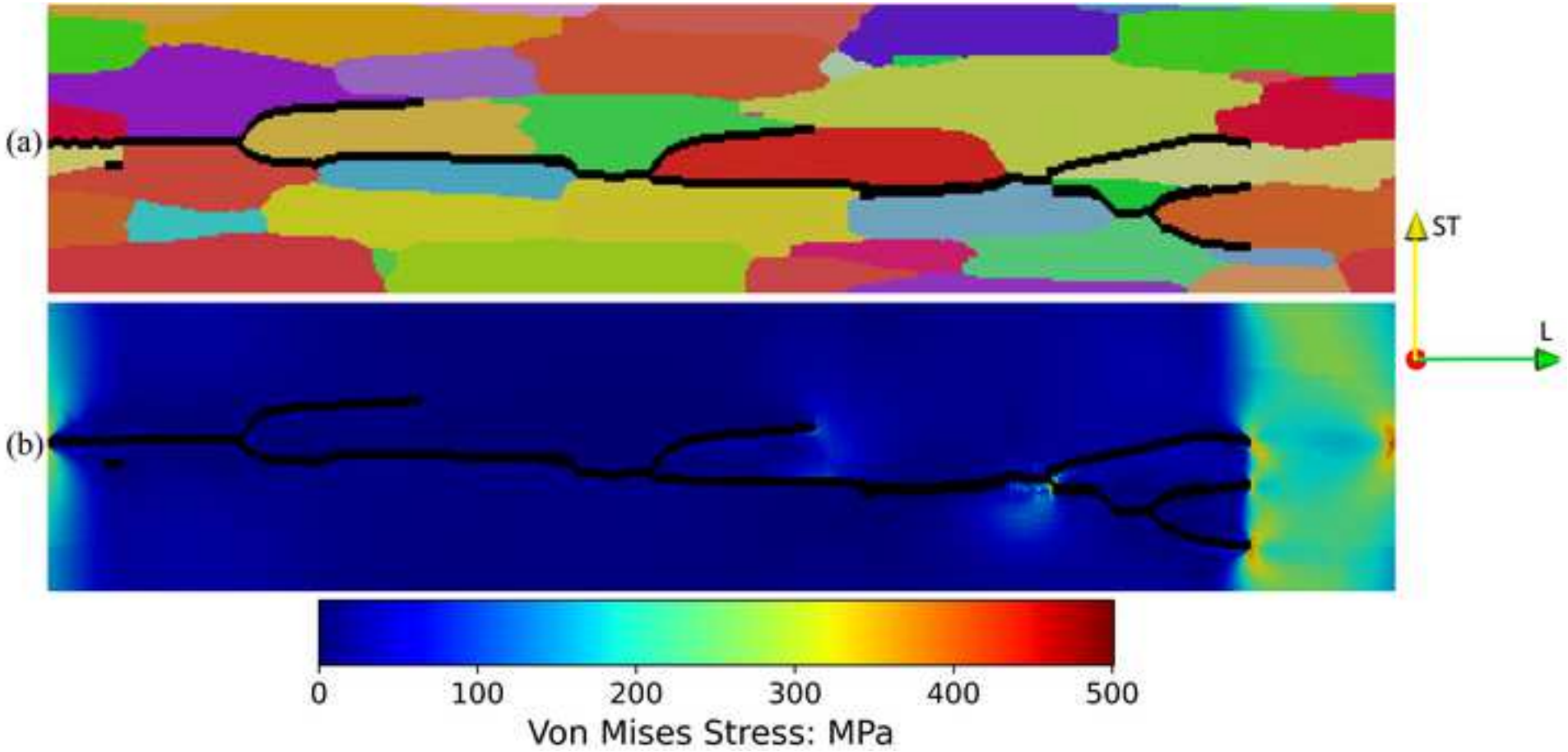

Figure

Click here to access/download;Figure;Figure 7.png

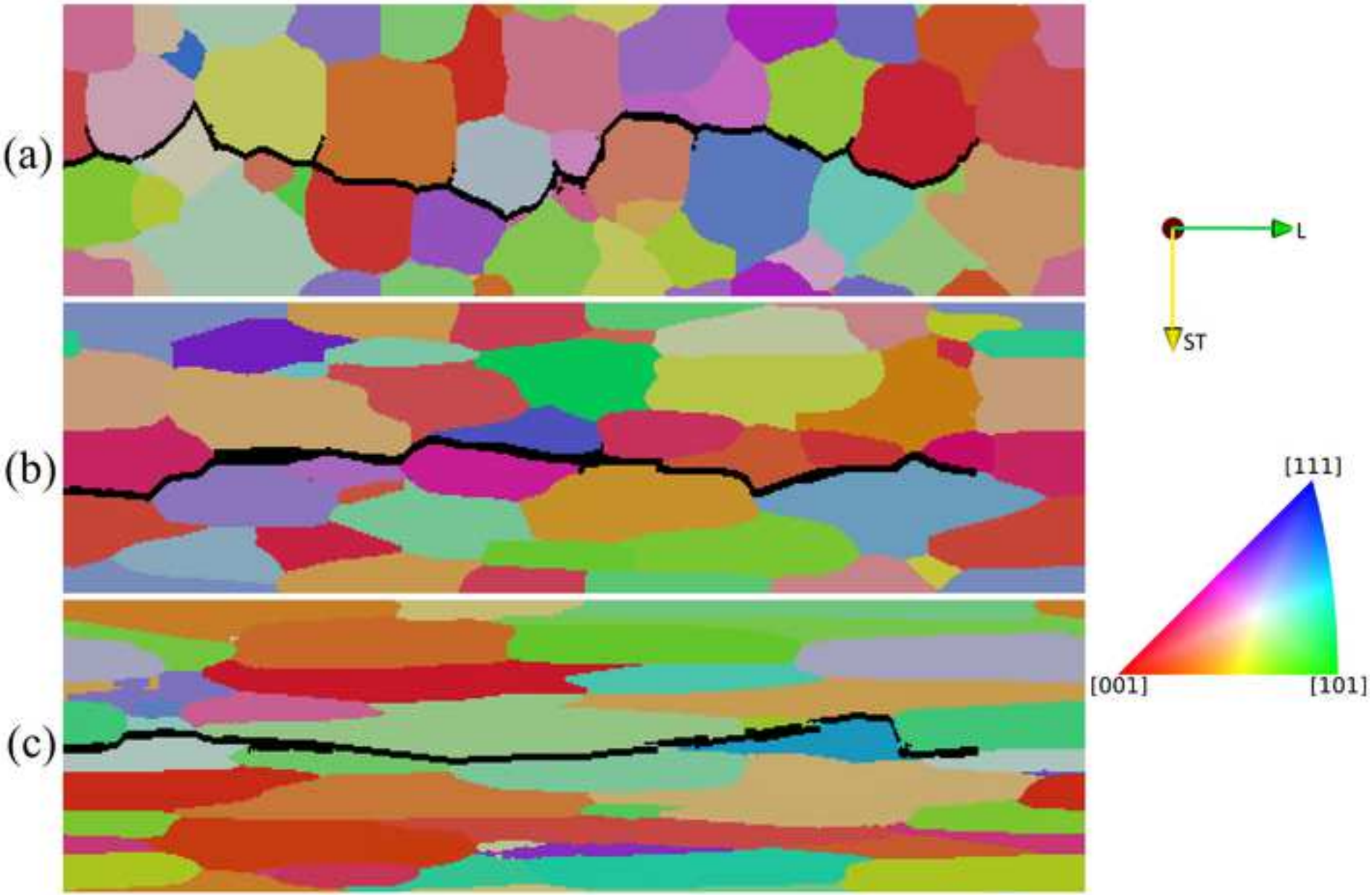

Figure

Click here to access/download;Figure;Figure 8.png

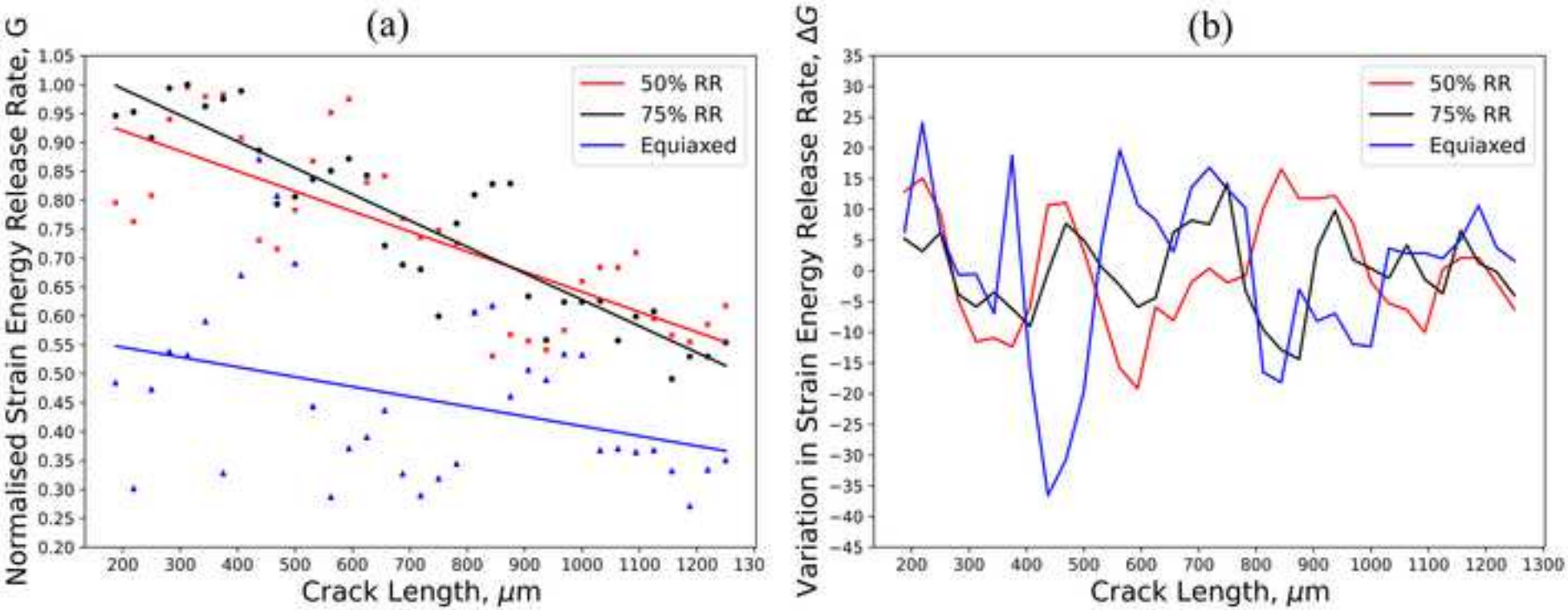

Figure

Click here to access/download;Figure;Figure 9.png

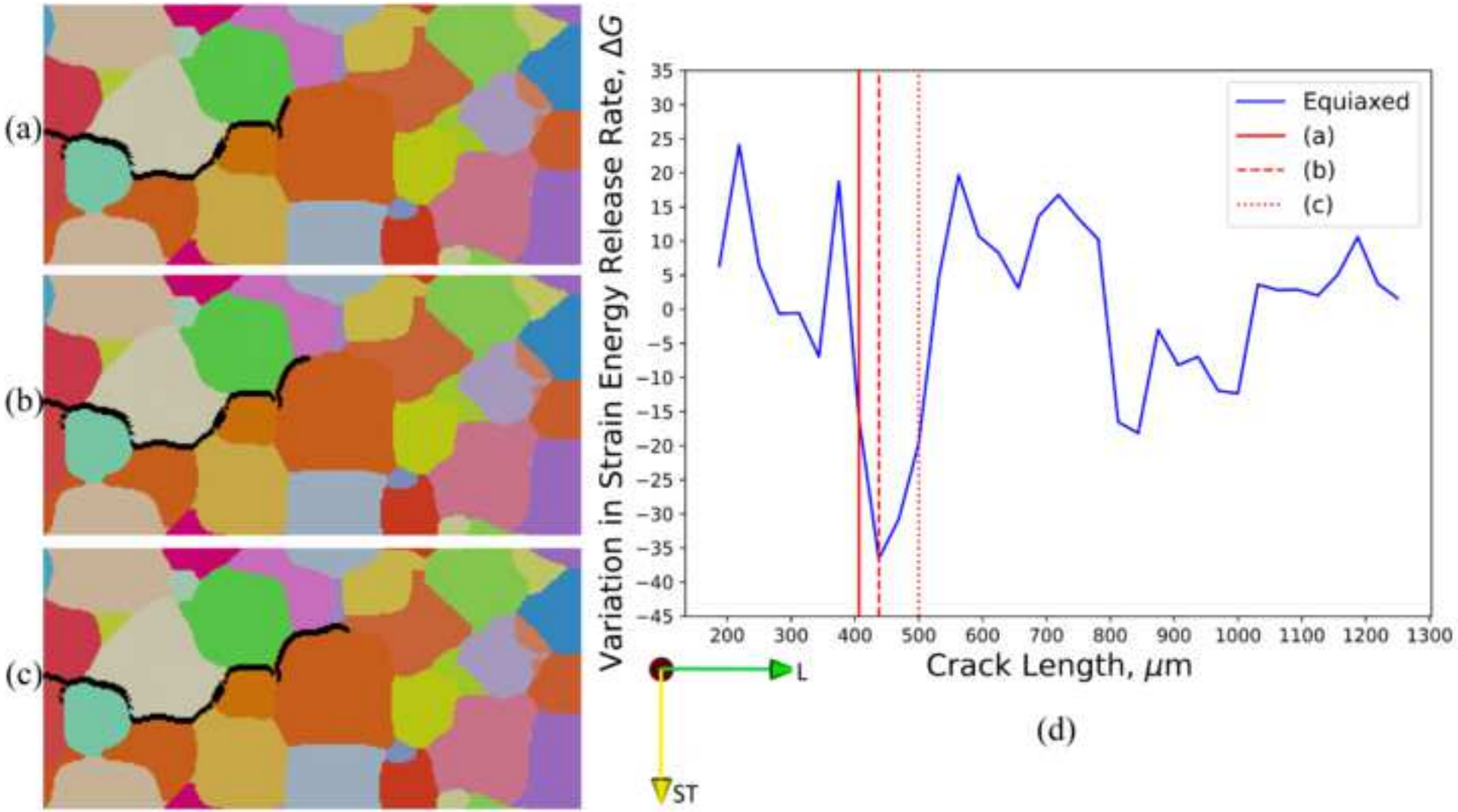

Figure

Click here to access/download;Figure;Figure 10.png

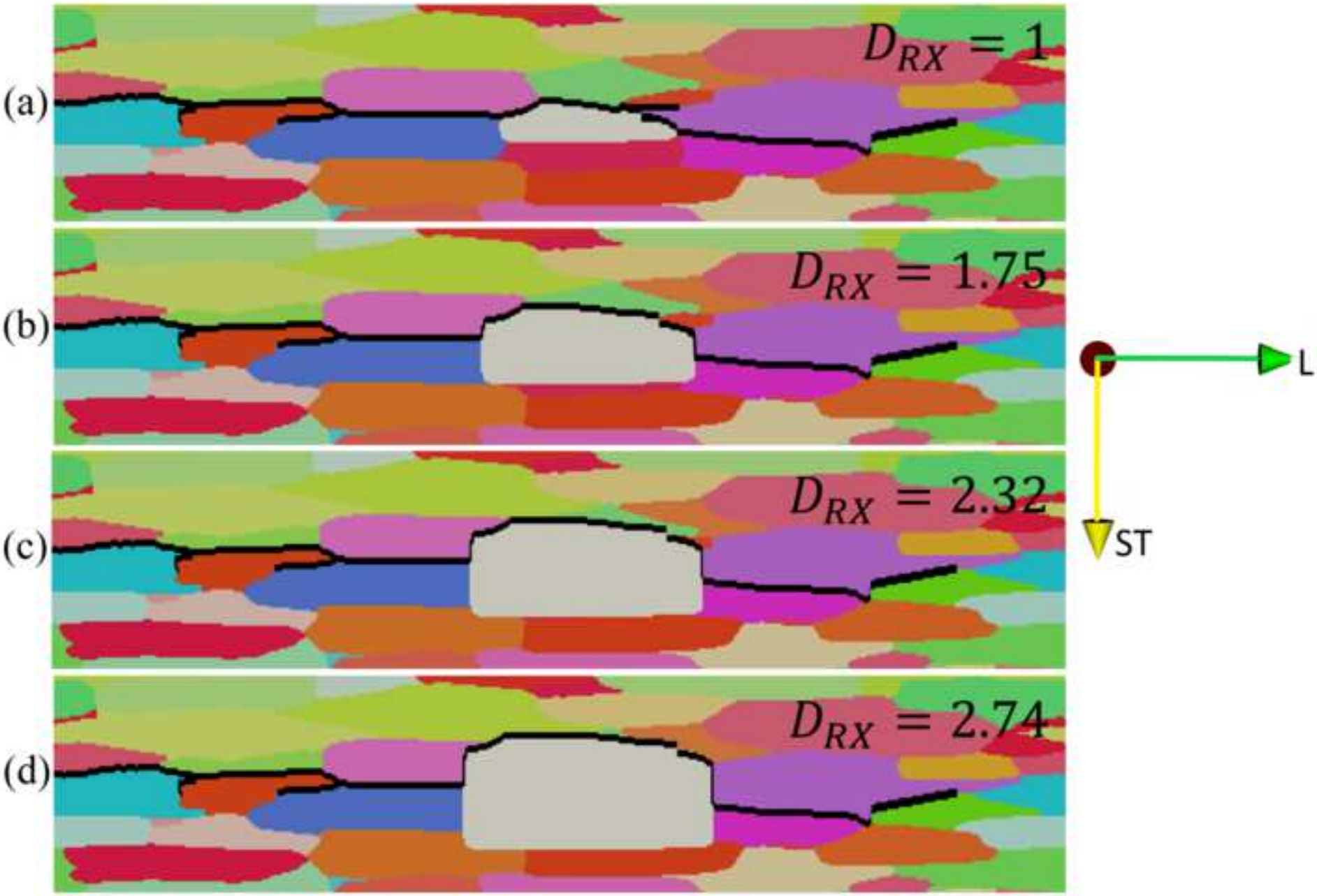

Figure

Click here to access/download;Figure;Figure 11.png

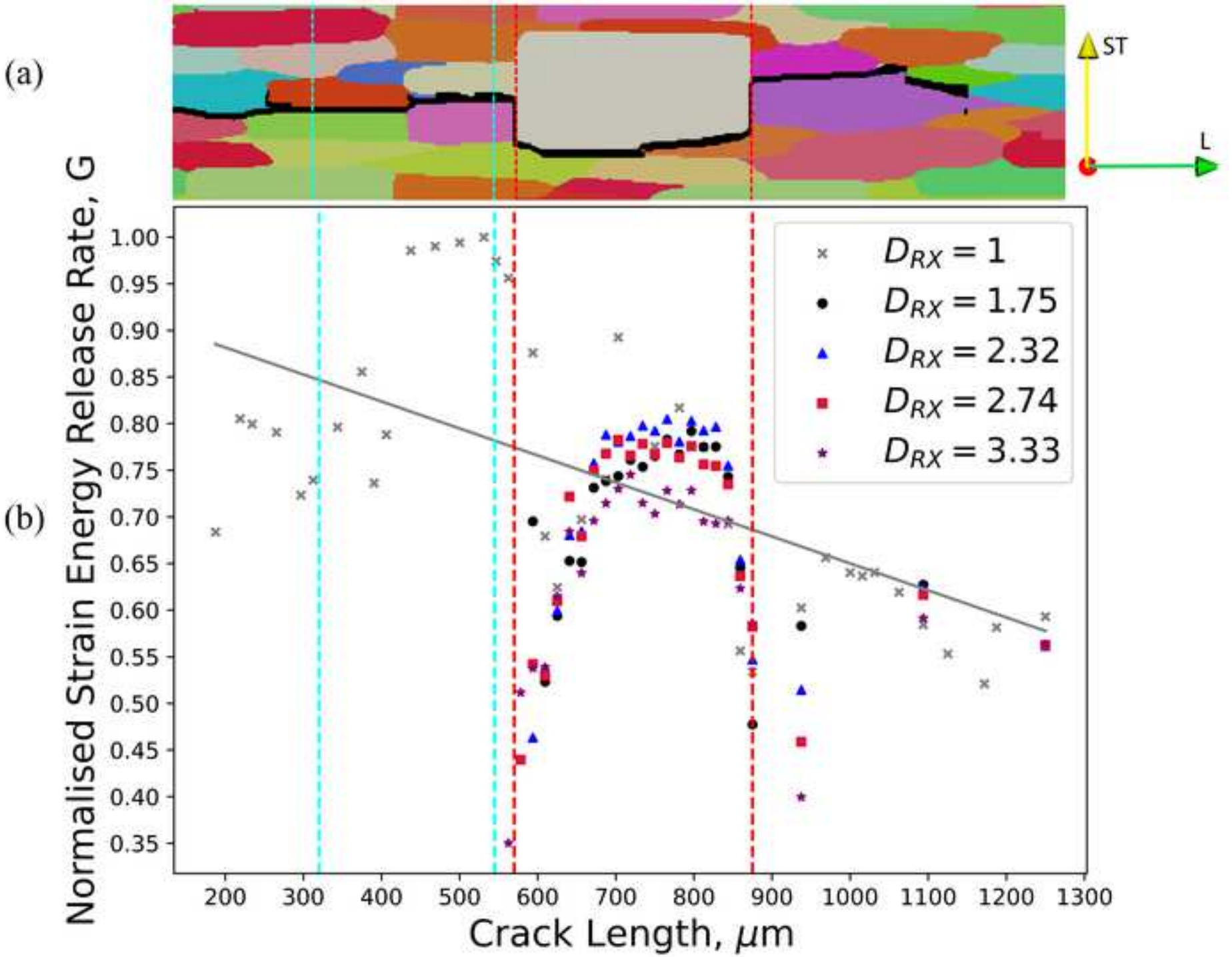

Graphical Abstract

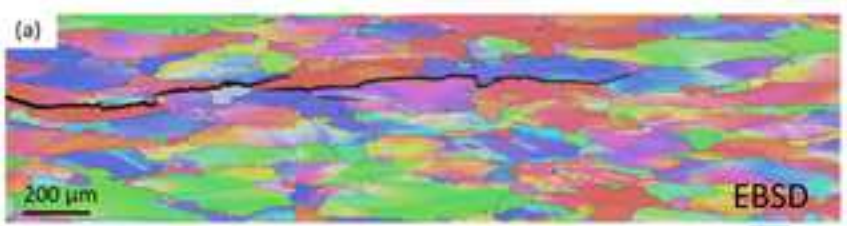

EBSD data is used to create synthetic grain structures for the CP model. Cracks can be seen in black.

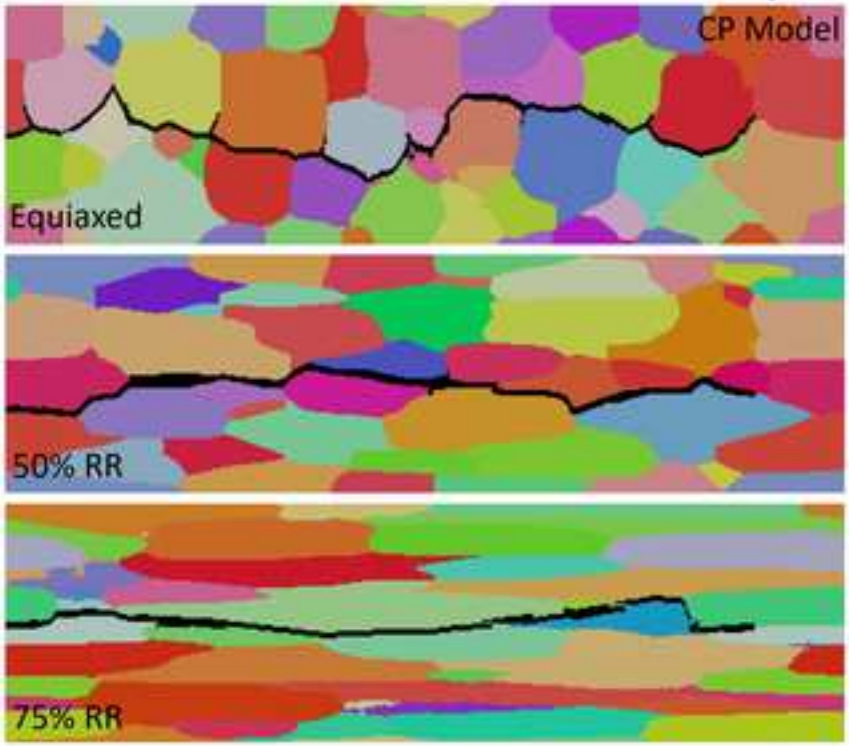

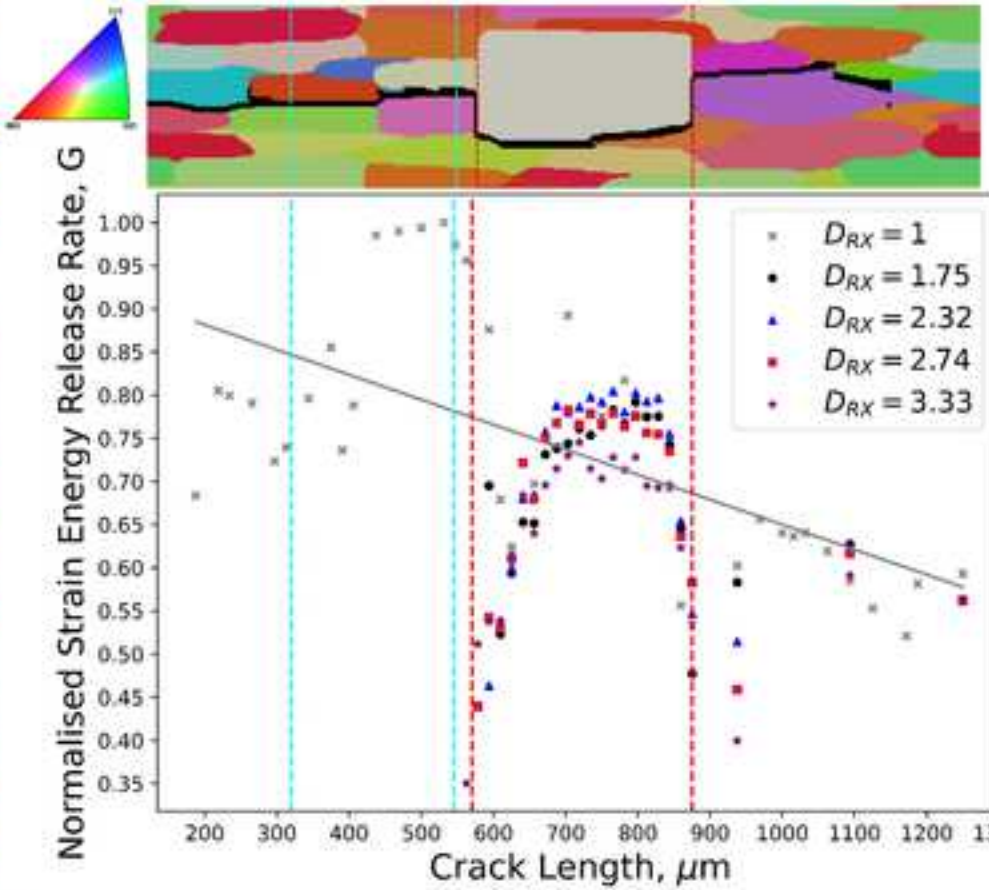

Comparison of the effect of embedding a single recrystallized grain in the centre of the grain structure VE with increasing size relative to the matrix (D_{RX}), on the relative strain energy release rate, G_n. Larger D_{RX} ratio values can be seen to cause a larger decrease in G.

Declaration of interests

☒ The authors declare that they have no known competing financial interests or personal relationships that could have appeared to influence the work reported in this paper.

☐The authors declare the following financial interests/personal relationships which may be considered as potential competing interests: